Bjerknes forces between two bubbles. Part 1. Response to a step change in pressure

By NIKOLAOS A. PELEKASIS
AND JOHN A. TSAMOPOULOS

Department of Chemical Engineering, State University of New York at Buffalo, Buffalo,
NY 14260, USA

It is well known from experiments in acoustic cavitation that two bubbles pulsating in a liquid may attract or repel each other depending on whether they oscillate in or out of phase, respectively. The forces responsible for this phenomenon are called 'Bjerknes' forces. When attractive forces are present the two bubbles are seen to accelerate towards each other and coalesce (Kornfeld & Suvorov 1944) and occasionally even breakup in the process. In the present study the response of two initially equal and spherical bubbles is examined under a step change in the hydrostatic pressure at infinity. A hybrid boundary–finite element method is used in order to follow the shape deformation and change in the potential of the two interfaces. Under the conditions mentioned above the two bubbles are found to attract each other always, with a force inversely proportional to the square of the distance between them when this distance is large, a result known to Bjerknes. As time increases the two bubbles continue accelerating towards each other and often resemble either the spherical-cap shapes observed by Davies & Taylor (1950), or the globally deformed shapes observed by Kornfeld & Suvorov (1944). Such shapes occur for sufficiently large or small values of the Bond number respectively (based on the average acceleration). It is also shown here that spherical-cap shapes arise through a Rayleigh–Taylor instability, whereas globally deformed shapes occur as a result of subharmonic resonance between the volume oscillations of the two bubbles and certain non-spherical harmonics (Hall & Seminara 1980). Eventually, in both cases the two bubbles break up due to severe surface deformation.

1. Introduction

More than a century ago C. A. Bjerknes and his son V. F. K. Bjerknes discovered a very interesting hydrodynamic effect, namely that pulsating bodies in fluids either attract each other when they oscillate in phase or repel each other when they oscillate out of phase. In order to explain this phenomenon they postulated that every body that is immersed or moving in an accelerating fluid is subject to a kinetic buoyancy equal to the product of the acceleration of the fluid multiplied by the mass of fluid displaced by the body. In the case of two interacting bubbles each one of them moves due to fluid acceleration caused by the oscillations of the other one. They also measured the force, which they found to be inversely proportional to the square of the distance between the bubbles (Bjerknes 1906, 1909). Naturally they made the analogy with electromagnetism and they coined the terms 'hydroelectricity' and 'hydromagnetism'. Hicks (1879, 1880) independently obtained an analytical expression for the force between pulsating spheres using the method of images in an effort to explain gravitation. Pearson (1884)

also derived independently an analytical expression of this force and tried to explain magnetism based on the mutual attraction or repulsion due to pulsation.

More recently the problem of bubble–bubble interaction has been addressed again, but now in the context of gas–liquid separation in bubbly fluids and in cavitation observed in high-speed flows. In particular, Kornfeld & Suvorov (1944) in their study of cavitation observed that pressure variations induced bubble formation close to solid surfaces followed by radial vibration of the bubbles. Very frequently two bubbles were seen to approach each other with constantly increasing velocity and coalesce to form larger bubbles. In other cases, they were seen to repel each other or, when their sizes differed significantly, the smaller one began to revolve around the larger one in a circular or elliptical orbit. For large pressure variations and after reaching a certain size the bubbles were observed to deform significantly, break up and collide with the solid surfaces at a great speed after following a zig-zag trajectory. These are often referred to as 'dancing bubbles'. The present study offers quantitative arguments for the onset of instabilities that lead to bubble breakup and in Part 2 of this study (Pelekasis & Tsamopoulos 1993) it is shown how bubble interaction can affect or even instigate the zig-zag motion.

It is also well known that a standard pressure wave can be used for trapping bubbles in a liquid (Blake 1949). Eller (1967) observed that bubbles smaller than the resonant size have a stable equilibrium position close to pressure maxima (antinodes). Once two bubbles reach this area and approach each other they suddenly accelerate towards each other and coalesce, forming a larger bubble. This process continues until the bubble exceeds the resonant size in which case it is driven away from the antinode, often leaving smaller bubbles behind it. Bubbles larger than the resonant size migrate towards pressure minima (nodes) where they form larger bubbles through coalescence. However, there appears to be an upper limit beyond which bubbles cannot grow (Blake 1949). Blake attributes this to the same effect that caused bubble breakup in the experiments conducted by Kornfeld & Suvorov, i.e. the domination of inertia forces over surface tension.

The localization of bubbles at the 'nodes' of a pressure wave occurs when the Bjerknes force on them balances the usual buoyancy force caused by gravity. This type of Bjerknes force is due to the acceleration of fluid induced by the externally imposed pressure gradient. This is the primary effect. The force responsible for attraction or repulsion between pulsating bubbles is much weaker since it is a secondary effect. More specifically, a small variation in the acoustic pressure induces pulsations to each one of the bubbles which then radiates a pressure wave towards the other one. This secondary sound field causes the two bubbles to accelerate. Based on this reasoning, Crum (1974) used a stationary pressure wave in the vertical direction to trap the bubbles and induce volume oscillations. Then he measured their relative velocity of approach in the horizontal direction. The secondary Bjerknes force between two bubbles is much smaller than the primary one. In particular, using a linearized potential flow model he found the secondary force between two spherical bubbles of equal size, at a distance of four radii apart and oscillating with a frequency 377 Hz, to be less than half the force due to the primary acoustic field. However, the secondary force increases with increasing frequency of the pulsations and ultrasonic pressure variations in a liquid may be used to clear it from gas bubbles; see Batchelor (1967).

The goal here is to obtain a quantitative and detailed description of the dynamics of some of the phenomena presented above. In particular, the mechanism leading to coalescence will be explained, the instabilities during deformation and prior to breakup will be identified, and finally the relevant time and space scales for the evolution of the

effects mentioned above will be obtained. To this end, the response of two initially spherical bubbles, immersed in an inviscid and incompressible liquid, will be examined. The bubbles will be subject to a step change in pressure at infinity. Shape deviations from sphericity will be allowed and no *a priori* assumptions on the velocity potential will be made, in contrast to Oguz & Prosperetti (1990). Since the far-field pressure remains constant in time its frequency is zero and both bubbles are driven below their resonance-frequency. Consequently, they will always attract each other irrespective of their relative size, in the absence of any initial velocity field. The effect of an oscillatory pressure variation at infinity and the subsequent repulsion or attraction between two bubbles depending on their relative size is discussed in the second part of this study.

The assumption of potential flow is justified in this problem since $Re \gg 1$ for water and most common fluids, and for relatively large bubbles of radius of the order of 1 mm or larger. Consequently, results will be valid in a timescale $t < Re^{\frac{1}{2}}$ which is the time needed for vorticity to diffuse from the two interfaces and through the boundary layers to the main body of the fluid. As the two bubbles approach each other the distance between them becomes the relevant characteristic lengthscale. As a result, Re decreases significantly and viscous forces soon become important for a short period of time before coalescence. It should also be noted that for a boundary layer on a free surface the flow may separate only when the curvature of the free surface becomes very large. Hence, formation of standing eddies close to the two interfaces is unlikely to happen and the flow can be safely assumed to be irrotational in the entire domain of the liquid. Finally, a measure of the relative importance of buoyancy and surface tension is given by the gravitational Bond number, $Bo = (gR^{*2}\rho)/\sigma$, where g here is the gravitational acceleration, R^* is the bubble radius, ρ the density of the fluid and σ is the surface tension. For gas bubbles with radius of the order of 1 mm, surrounded by water at 20 °C, the gravitational Bo_g is roughly 0.13. Hence gravity can be neglected.

As will become evident in the following sections, the motion of the two bubbles exhibits significantly different features as time or nonlinearities increase. As a result, the linear problem and the initial stages of the motion can be studied more conveniently and accurately using bispherical coordinates in an Eulerian framework. Thus, the two interfaces are uniquely described, at least in the early stages of motion. However, as the two centres of mass move with an increasing velocity, the description of the interfaces becomes inaccurate or even impossible in the original coordinate system, since single-valuedness may be lost. Hence, a Lagrangian representation is used for the description of highly deformed shapes obtained before coalescence.

In §§2.1 and 2.2 the Eulerian and mixed Eulerian–Lagrangian representation of the motion is given, and the canonical variables of the Hamiltonian formulation are introduced as explained in Pelekasis, Tsamopoulos & Manolis (1991, referred to as PTM1). In the mixed Eulerian–Lagrangian representation, the position of the free surfaces and the velocity potential on them are updated following Lagrangian particles; whereas Laplace's equation is used to relate the potential flux to the potential on the two interfaces. In §2.3 an integral formulation is presented using Green's theorem. This leads to an integral equation of the first kind. In the absence of viscosity the motion is conservative. Formulae for the energy of the system along with other conserved quantities are given in §2.4 and are used frequently as accuracy tests of the calculations.

In §3 the numerical method of solution is briefly outlined. More details are given in Pelekasis, Tsamopoulos & Manolis (1992, referred to as PTM2). It involves hybridization of the boundary element method, used for the discretization of the integral equation, and the finite element method, used for the kinematic and dynamic

boundary conditions. With the Lagrangian representation the collocation method is used for the discretization of the kinematic and dynamic conditions. It is shown that both the Eulerian and the mixed Eulerian–Lagrangian schemes fail at about the same point in time. Upon exhaustive numerical simulations it is found that this is not a numerical artifact, but it is caused by a physical instability.

Next, the linear problem is solved in §4 for equal and unequal bubbles. The eigenfrequencies and eigenfunctions are found by direct eigenvalue calculations. Then the non-homogeneous problem is solved with a forcing term due to a step change in pressure at infinity. Solving the linear problem became necessary not only for checking the rest of the numerical results and reporting the eigenvalues of this problem for the first time, but also for identifying the relevant timescales of the motion and explaining and classifying the nonlinear results. To this end, the Eulerian formulation is the most suitable one, along with bispherical coordinates, since in the linear limit the two bubbles are nearly spherical and this is the only known coordinate system in which two neighbouring spheres can be coordinate surfaces.

In §5 the full nonlinear problem is studied, the asymptotic results obtained by previous investigators are recovered and the motion of two equal bubbles is monitored until computations fail at a finite time due to formation of regions of very high curvature. Two different types of shape are observed depending on the Bond number based on the average acceleration of each bubble, $(\langle g^* \rangle R^{*2} \rho)/\sigma$. When the Bond number is below a critical range shapes that are deformed throughout the interface appear as a result of subharmonic resonance (Hall & Seminara 1980). Such shapes were first reported by Kornfeld & Suvorov (1944). Beyond this critical range a Rayleigh–Taylor type of instability occurs that gives rise to spherical-cap shapes. This characterization is given in analogy with the shapes observed experimentally by Davies & Taylor (1950) in rising bubbles. The effect of pressure on the dynamic behaviour of the system is studied in §6 and it is seen that increasing the static pressure results in increased values of the critical Bond number. Finally, conclusions are drawn in §7.

2. Problem formulation

Nonlinear interactions between two gas bubbles surrounded by an inviscid and incompressible fluid are studied. The flow is irrotational and, for simplicity, axisymmetry around the axis connecting the centres of mass of the two bubbles is assumed. The density of the gas inside the bubbles is assumed to be much smaller than that of the liquid ρ, so that the gas is considered to be inertialess. Therefore, its pressure varies only with time according to a polytropic law.

Both bubbles are initially spherical in shape with dimensional radii R_1^* and R_2^* and distance D^* between the two centres. The radius R_1^* of the bubble on the left is assigned as the characteristic length of the system. Thus the two dimensionless bubble radii and their distance are $R_1 \equiv 1$, $R_2 \equiv R_2^*/R_1^* \equiv R$ and D, respectively. For convenience the bubble on the left is assumed to be the larger one of the two, i.e. $R \leqslant 1$, and also $D > 1 + R$. Since the only means of distinguishing between the two bubbles is their initial radius, solutions when $R > 1$ can be readily obtained from solutions given here. The surface tension, σ, between the two gas/liquid interfaces is used for making pressure dimensionless, $P \equiv P^*/(2\sigma/R_1^*)$. The initial hydrostatic pressure in the liquid, P_s, is used as a pressure datum and can also be thought of as a Weber number measuring the relative importance of inertia and surface tension forces. In the absence of a characteristic velocity, surface tension may be used to make the velocity potential and time dimensionless, $\Phi = \Phi^*/(\sigma R_1^*/\rho)^{\frac{1}{2}}$, $t = t^*/(\rho R_1^{*3}/\sigma)^{\frac{1}{2}}$. The physical problems to
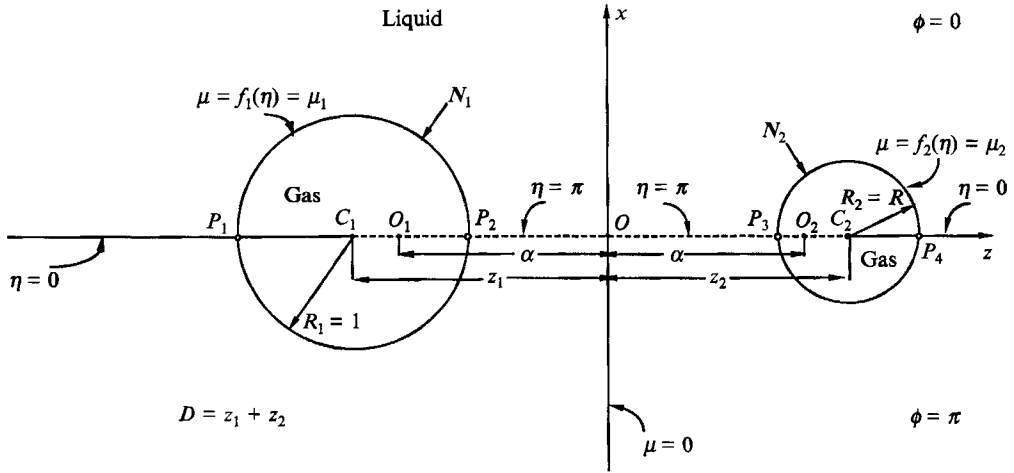
FIGURE 1. Schematic of the representation of the two bubbles in bispherical coordinates.

be solved in both this and the companion paper (Part 2) will be formulated here in the interest of space, and only the important differences will be mentioned in each case specifically. Here, the motion in the fluid is induced by a step change in pressure at infinity. This condition requires that for time greater than zero the pressure at infinity is given by

$$P_\infty = P_s(1 + \epsilon), \qquad (2.1)$$

where ϵ is a measure of the disturbance. Besides this change, the two interfaces remain initially spherical and no initial velocity is imparted to the system, which guarantees irrotationality of the motion.

2.1. *Eulerian formulation*

In order to represent (at least initially) both free surfaces as single-valued functions using one coordinate system, bispherical coordinates are used. The equations solved on each interface are similar to those used in the case of an oscillating shell surrounding a compressible bubble (see PTM1). They are adapted here for the different geometry and coordinate system. A schematic of the two bubbles at $t = 0$ is given in figure 1. C_1 and C_2 are the centres of the two spherical bubbles, O is the origin of the bispherical coordinate system and O_1 and O_2 are its two poles. $C_1 O = z_1 < 0$ and $C_2 O = z_2 > 0$ are the coordinates of C_1 and C_2 with respect to O, whereas the distance of each coordinate pole from O is α. The origin and the poles are chosen in such a way that the two bubbles are coordinate surfaces of the coordinate system at $t = 0$. Each point in space is now described via the bispherical coordinates (μ, η, ϕ), where ϕ is the same polar angle used in spherical and cylindrical coordinates, whereas μ and η are related to the Cartesian coordinates (x, y, z) as

$$z = \frac{\alpha \sinh \mu}{\cosh \mu - \cos \eta}, \quad x = \frac{\alpha \sin \eta \cos \phi}{\cosh \mu - \cos \eta}, \quad y = \frac{\alpha \sin \eta \sin \phi}{\cosh \mu - \cos \eta}. \qquad (2.2)$$

In this coordinate system $0 \leqslant \eta \leqslant \pi$, $-\infty \leqslant \mu \leqslant \infty$, and the segment of the z-axis with $|z| < \alpha$ is represented by $\eta = \pi$ whereas the remaining z-axis, $|z| > \alpha$, is represented by $\eta = 0$. In general μ will be a function of η on each free surface; $\mu = f_1(\eta, t)$ on the left bubble, whereas $\mu = f_2(\eta, t)$ on the right bubble. However, at $t = 0$ each surface is

spherical and μ becomes a constant; $\mu = \mu_1, \mu_2$ on the left and right bubble respectively. For more details see Morse & Feshbach (1953); μ_i, α and z_i are given as functions of D and R in Pelekasis (1991).

Since only axisymmetric disturbances are considered, calculation of the bounding surfaces reduces to calculation of the generating curves of the two bubbles. Further, on applying Green's theorem to Laplace's equation, an integral equation relating the potential to the flux on the boundary is obtained. This procedure is described in §2.3. Schematically the resulting relationship can be written as

$$ L\left(\varPsi_1, \varPsi_2, \frac{\partial\varPhi}{\partial\zeta_1}, \frac{\partial\varPhi}{\partial\zeta_2}\right) = 0, \tag{2.3} $$

where $\varPsi_i$, $\partial\varPhi/\partial\zeta_i (i = 1, 2)$ are respectively the values of the potential and the flux normal to the interface, for the two bubbles. They are defined as:

$$ \varPsi_i = \varPhi(\mu = f_i(\eta, t), \eta, t), \quad i = 1, 2, \tag{2.4} $$

$$ \frac{\partial\varPhi}{\partial\zeta_i} = \boldsymbol{\nabla}\varPhi \cdot \boldsymbol{N}_i, \quad i = 1, 2, \tag{2.5} $$

with $N_i (i = 1, 2)$ being the outward-pointing normal vectors with respect to the liquid; i.e. they point towards the interior of the two bubbles. In bispherical coordinates

$$ \boldsymbol{N}_i = \boldsymbol{e}_\mu \frac{(-1)^i}{(1+f_{i\eta}^2)^{\frac{1}{2}}} + \boldsymbol{e}_\eta \frac{(-1)^{i+1}f_{i\eta}}{(1+f_{i\eta}^2)^{\frac{1}{2}}}, \quad i = 1, 2, \tag{2.6} $$

where η as a subscript denotes partial differentiation and $\boldsymbol{e}_\mu, \boldsymbol{e}_\eta$ are the unit vectors in bispherical coordinates. Since the kinematic and dynamic boundary conditions are also written on the boundary, the formulation may be recast in terms of the surface quantities, $f_i, \varPsi_i, \partial\varPhi/\partial\zeta_i (i = 1, 2)$ that depend only on time and one spatial coordinate, namely η. This makes the one-dimensional nature of this problem apparent and facilitates numerical differentiation.

Proceeding along the same lines as in PTM1, the above surface variables are introduced in the kinematic and dynamic boundary conditions, which now read as

$$ \frac{\partial f_i}{\partial t} = (-1)^i \frac{\cosh f_i - \cos \eta}{\alpha}(1+f_{i\eta}^2)^{\frac{1}{2}}\frac{\partial\varPhi}{\partial\zeta_i}, \quad \mu = f_i(\eta, t), \quad 0 \leqslant \eta \leqslant \pi, \quad i = 1, 2, \tag{2.7} $$

$$ \frac{\partial\varPsi_i}{\partial t} = 2P_\infty - 2P_{ig} + \frac{1}{2}\left(\frac{\partial\varPhi}{\partial\zeta_i}\right)^2 - 2\mathscr{H}_i - \frac{1}{2h^2(1+f_{i\eta}^2)}\left(\frac{\partial\varPsi_i}{\partial\eta}\right)^2 $$

$$ + (-1)^i \frac{\partial\varPhi}{\partial\zeta_i}\frac{\partial\varPsi_i}{\partial\eta}\frac{f_{i\eta}}{h(1+f_{i\eta}^2)^{\frac{1}{2}}}, \quad \mu = f_i(\eta, t), \quad 0 \leqslant \eta \leqslant \pi, \quad i = 1, 2, \tag{2.8} $$

where $P_{ig} (i = 1, 2)$ denote the pressures inside the two bubbles, h is the same metric along both μ- and η-directions and $\mathscr{H}_i (i = 1, 2)$ are the mean curvatures on the two interfaces defined as

$$ -2\mathscr{H}_i \equiv \boldsymbol{\nabla}\cdot(-N_i) $$

$$ = (-1)^i\left[\frac{f_{i\eta\eta}}{h(1+f_{i\eta}^2)^{\frac{3}{2}}} + \frac{2f_{i\eta}\,\partial h/\partial\eta}{h^2(1+f_{i\eta}^2)^{\frac{1}{2}}} - \frac{2\,\partial h/\partial\mu}{h^2(1+f_{i\eta}^2)^{\frac{1}{2}}} + \frac{f_{i\eta}\cot\eta}{h(1+f_{i\eta}^2)^{\frac{1}{2}}}\right], \quad i = 1, 2. \tag{2.9} $$

For the air/water system the rate of change of the internal energy of each bubble is larger than the rate of heat transfer to/from the liquid. Thus, if uniform conditions

exist inside each bubble the pressure varies adiabatically with the instantaneous volume (Plesset & Hsieh 1960). Thus,

$$P_{i,g}(t) = \left(P_s + \frac{1}{R_i}\right)\left(\frac{\frac{4}{3}\pi R_i^3}{V_i(t)}\right)^\gamma, \quad i = 1, 2, \tag{2.10}$$

where γ is the polytropic constant, $1 \leqslant \gamma \leqslant 1.4$, and V_i denotes the dimensionless volume of each bubble; for an adiabatic process $\gamma = 1.4$. Expressions for the metric h and the volume V_i in bispherical coordinates are given in Pelekasis (1991). Owing to axisymmetry,

$$\frac{\partial f_i}{\partial \eta} = \frac{\partial \Psi_i}{\partial \eta} = \frac{\partial^2 \Phi}{\partial \eta \, \partial \zeta_i} = 0 \quad \text{at} \quad \eta = 0, \pi. \tag{2.11}$$

It should also be noted that the shape of the free surfaces and the velocity potential evaluated on them were shown by Miles (1977) and Zakharov (1968) to be the canonical variables of the Hamiltonian formulation for gravity water waves. Hence, there is every indication that they are the most appropriate variables for the description of the motion in this problem as well. More recently Benjamin (1987) used the same approach in deriving the Hamiltonian theory and integral invariants for the motion of bubbles in an infinite liquid.

2.2. *Mixed Eulerian–Lagrangian formulation*

During the last stages of motion and shortly before coalescence, both interfaces are expected to deform severely. In order to capture such behaviour it is advantageous to follow Lagrangian particles as they move in time. As a result of axisymmetry only one parameter is needed to label different particles. The arclength, s, along each interface would be a possible choice but its value on each particle varies with time. This makes it inconvenient to use in numerical integration and differentiation. Hence, particles are labelled using a parameter ξ that varies from 1 to N on each one of the N particles (see also Longuet-Higgins & Cokelet 1976). The relationship between the arclength s and ξ is given below. Two local spherical coordinate systems are used for the description of the two free surfaces. Initially, the origin of each of them coincides with the centre of each of the bubbles.

The arrangement mentioned above is used for updating the shape and potential of the two interfaces. This is advantageous for the description of the motion, especially for discretization of the kinematic and dynamic boundary conditions when the initial distance between the two bubbles is large, because it prohibits the generation of large numbers. For the integral equation, which is used to calculate solutions to Laplace's equation, another spherical coordinate system is employed. It is common to both bubbles and is convenient for integration along the two free surfaces even when they are far apart. Its origin lies in the middle of the line segment joining the nearest surfaces of the two bubbles, along the axis of symmetry z, at $t = 0$. This system does not have to be relocated, irrespective of the relative position of the two bubbles, and from now on it will be referred to as the global spherical coordinate system.

This formulation uses ideas from both the Eulerian and Lagrangian approaches for describing the motion. In particular, the kinematic and dynamic boundary conditions are expressed in terms of the rates of change of the potential and the coordinates, following a fixed particle. However, in order for the velocity to be determined on the interfaces the normal derivative of the potential is also needed. The relationship between the potential and its normal derivative on the boundary is provided by the integral form of Laplace's equation. Hence, the method is called mixed Eulerian–Lagrangian (see also Longuet-Higgins & Cokelet 1976).
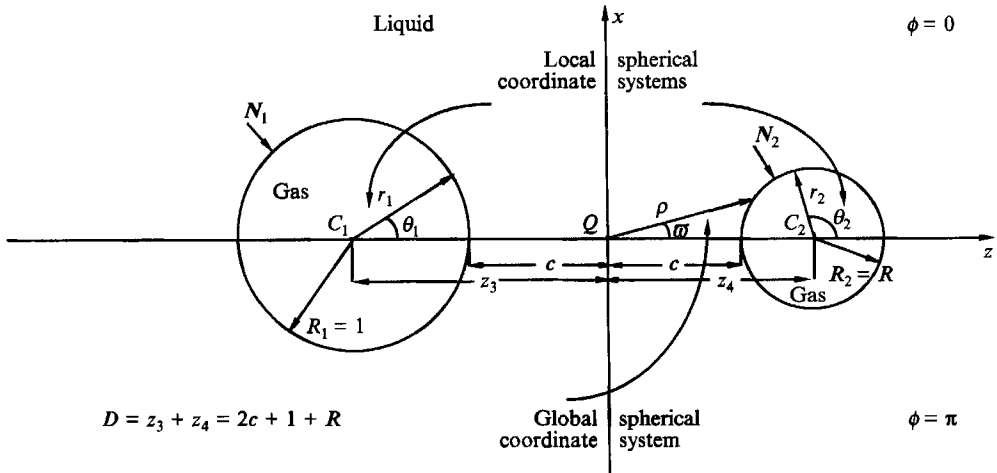
FIGURE 2. Schematic of the representation of each individual bubble in a local spherical coordinate system, as well as the representation of the entire system in a global spherical coordinate system.

The schematic in figure 2 shows again the two bubbles and the location of the coordinate systems at $t = 0$. Q is the origin of the global coordinate system whereas C_1 and C_2 are the origins of the two local coordinate systems. $C_1 Q = z_3 < 0$ and $C_2 Q = z_4 > 0$ are the coordinates of C_1 and C_2 with respect to Q along the axis of symmetry. A point (ρ, ϖ, ϕ) in the global coordinate system can be represented in terms of the coordinates (r_1, θ_1, ϕ) of the local coordinate system based on the left bubble as

$$\rho = [(z_3 + r_1 \cos \theta_1)^2 + r_1^2 \sin^2 \theta_1]^{\frac{1}{2}}, \tag{2.12}$$

$$\varpi = \tan^{-1} \left(\frac{r_1 \sin \theta_1}{z_3 + r_1 \cos \theta_1} \right), \tag{2.13}$$

and similarly for (r_2, θ_2, ϕ). The components (v_ρ, v_ϖ) of any vector in the global coordinate system are given, in terms of its decomposition (v_r, v_θ) in either one of the two local coordinate systems, in Pelekasis (1991).

The kinematic condition on the two interfaces equates the velocity of every point on the surface with that of the fluid particle residing there, namely

$$\mathbf{u} = \nabla \Phi, \tag{2.14}$$

$$\frac{D\mathcal{R}_i}{Dt} = U_i, \quad i = 1, 2, \tag{2.15}$$

where $\mathbf{u}$ is the fluid velocity, Φ is the velocity potential and U_i and $\mathcal{R}_i$ denote the particle velocity and position on the two interfaces.

The evolution of the velocity potential of a fluid particle on the two free surfaces is given by combining Bernoulli's equation with the normal force balance,

$$D\Psi_i/Dt = \tfrac{1}{2}|U_i|^2 + 2P_\infty - 2P_{ig} - 2\mathcal{H}_i, \quad i = 1, 2. \tag{2.16}$$

Variables appearing in the above equation bear the significance ascribed to them in §2.1. Decomposing the velocity in the local coordinate systems and expressing the components in terms of the velocity potential yields

$$\frac{Dr_i}{Dt} = \frac{\Psi_{i\xi} r_{i\xi} - (\partial \Phi / \partial \zeta_i) r_i \theta_{i\xi} (r_{i\xi}^2 + r_i^2 \theta_{i\xi}^2)^{\frac{1}{2}}}{r_{i\xi}^2 + r_i^2 \theta_{i\xi}^2}, \quad i = 1, 2, \tag{2.17}$$

$$\frac{D\theta_i}{Dt} = \frac{\Psi_{i\xi} r_i \theta_{i\xi} + r_{i\xi}(\partial\Phi/\partial\zeta_i)(r_{i\xi}^2 + r_i^2\theta_{i\xi}^2)^{\frac{1}{2}}}{r_i(r_{i\xi}^2 + r_i^2\theta_{i\xi}^2)}, \quad i = 1, 2, \tag{2.18}$$

$$\frac{D\Psi_i}{Dt} = \frac{1}{2}\left(\left(\frac{\partial\Phi}{\partial\zeta_i}\right)^2 + \frac{\Psi_{i\xi}^2}{r_{i\xi}^2 + r_i^2\theta_{i\xi}^2}\right) + 2P_\infty - 2P_{iq} - 2\mathscr{H}_i, \quad i = 1, 2, \tag{2.19}$$

where ξ as a subscript denotes partial differentiation. Expressions for the curvature and normal on each surface in the local coordinate systems are given in Pelekasis (1991).

It may be shown that the local coordinate, ξ, is related to the arclength along the surface of each bubble by

$$\partial s_i/\partial\xi = (r_{i\xi}^2 + r_i^2\theta_{i\xi}^2)^{\frac{1}{2}}, \quad i = 1, 2. \tag{2.20}$$

Owing to axisymmetry the derivatives with respect to ξ should satisfy the following conditions:

$$\frac{\partial r_i}{\partial\xi} = \frac{\partial\Psi_i}{\partial\xi} = \frac{\partial^2\Phi}{\partial\zeta_i\partial\xi} = 0 \quad \text{and} \quad \frac{\partial^2\theta_i}{\partial\xi^2} = 0 \quad \text{at} \quad \xi = 0, N, \quad i = 1, 2. \tag{2.21}$$

The last condition uniquely defines the interpolating function $\theta(\xi)$, to be represented in terms of the B-cubic splines which are introduced later. It is used in view of the equivalent condition, $\partial^2 s/\partial\theta^2 = 0$, which is satisfied in the Eulerian formulation.

2.3. *Formulation of the integral equation*

Applying Green's third identity to Laplace's equation results in an integral equation for the potential at a field point anywhere in the domain in terms of boundary values of the potential and its normal derivative. Allowing the field point to approach either of the two boundaries results in an integral equation which relates the potential on the two interfaces to its flux there, see PTM1 for details. Then, the integral equation takes the form

$$\tfrac{1}{2}\Phi(x', t) + \int_A \Phi(x, t)\frac{\partial\hat{G}}{\partial\zeta}(x, x')\,\mathrm{d}A(x, t) = \int_A \frac{\partial\Phi}{\partial\zeta}(x, t)\hat{G}(x, x')\,\mathrm{d}A(x, t), \tag{2.22}$$

where A is the surface area of both bubbles, $\hat{G}$ is the three-dimensional free-space singular solution of Laplace's equation subject to a point force at the source point x, and ζ increases along the normal to the boundary and outwards with respect to the domain, i.e. towards the interior of the bubbles. For an oscillating body the velocity potential and its normal derivative vanish at infinity like $1/r$ and $1/r^2$ respectively, r being the distance between the field point and some reference point. Thus the part of the two surface integrals in (2.22) taken at infinity equals zero. The integral on the left-hand side of (2.22) is understood in the Cauchy principal value sense. The singularity in this integral is integrated by a procedure similar to the one described in PTM1. Intermediate steps in evaluating surface integrals on each bubble are given in Pelekasis (1991).

Finally, for an axisymmetric problem the polar coordinate ϕ' of the field point may be set to zero. Integration along the polar coordinate, ϕ, of the source point yields

$$\Psi_i(q', t) + \sum_{j=1}^{2} \int_Q [\Psi_j(q, t) - \Psi_i(q', t)]\frac{\partial G}{\partial\zeta_j}(q, \beta, q', \beta')h_q h_\phi\,\mathrm{d}q$$

$$= \sum_{j=1}^{2} \int_Q \frac{\partial\Phi}{\partial\zeta_j}(q, t)G(q, \beta, q', \beta')h_q h_\phi\,\mathrm{d}q, \quad i = 1, 2, \tag{2.23}$$

where Q denotes the integration interval and

$$G = \int_0^{2\pi} \hat{G}\,\mathrm{d}\phi, \quad \frac{\partial G}{\partial\zeta_j} = \int_0^{2\pi} \frac{\partial\hat{G}}{\partial\zeta_j}\,\mathrm{d}\phi. \tag{2.24}$$

In the Eulerian formulation bispherical coordinates are used, hence

$$q = \eta, \quad q' = \eta', \quad \beta = \mu, \quad \beta' = \mu', \left.\begin{array}{c} \\ \\ \end{array}\right\}$$
$$h_q = h_\eta = \frac{\alpha(1+\mu_\eta^2)^{\frac{1}{2}}}{\cosh\mu - \cos\eta}, \quad h_\phi = \frac{\alpha\sin\eta}{\cosh\mu - \cos\eta}, \quad (2.25)$$

with $\mu = f_1(\eta, t)$ if $j = 1$ and $\mu = f_2(\eta, t)$ if $j = 2$. When $\hat{G} \equiv (1/4\pi)(1/|x - x'|)$ is written in bispherical coordinates, the two integrals in (2.24) can be written in terms of elliptic integrals (Pelekasis 1991).

In the mixed Eulerian–Lagrangian formulations the integrands appearing in (2.23) are expressed in the global spherical coordinates (ρ, ϖ, ϕ). Therefore,

$$q = \varpi, \quad q' = \varpi', \quad \beta = \rho, \quad \beta' = \rho', \quad h_q = h_\varpi = (\rho^2 + \rho_\varpi^2)^{\frac{1}{2}}, \quad h_\phi = \rho\sin\varpi, \quad (2.26)$$

with $j = 1$ and $j = 2$ at the left and right bubbles, respectively. When spherical coordinates are used the two kernels can again be written in terms of elliptic integrals (PTM1).

2.4. *Invariants of the motion*

In the absence of viscosity the system is conservative and therefore its total energy remains invariant with time. It consists of the kinetic and surface energy as well as the energy that the fluid exchanges with the two bubbles through their volume oscillations. Thus,

$$E = \frac{1}{2}\int_{A_1+A_2} \Phi\frac{\partial\Phi}{\partial\zeta}\,d(A_1+A_2) + \int_{A_1+A_2} d(A_1+A_2) + V_1\left(2P_\infty + \frac{2P_{1g}}{\gamma-1}\right) + V_2\left(2P_\infty + \frac{2P_{2g}}{\gamma-1}\right). \quad (2.27)$$

When the two bubbles have the same radius initially, i.e. $R = 1$, the plane perpendicular to the z-axis and at the midpoint of the line segment joining their centres is also a plane of symmetry. This midpoint is the centre of mass of the two bubbles and, owing to symmetry, remains so forever. The centres of mass of the two individual bubbles are given as

$$Z_i = \frac{\iiint_{V_i} z\,dV_i}{\iiint_{V_i} dV_i}, \quad i = 1, 2; \quad Z = \frac{Z_1 V_1 + Z_2 V_2}{V_1 + V_2}. \quad (2.28)$$

When the two radii are unequal the combined centre of mass, Z, varies with time.

Another quantity that varies with time, but can also be used as a check of the accuracy of numerical results, is the sum of the volumes of the two bubbles. In particular, it may be readily shown that the total volume change of both bubbles equals the sum of the integrals of the normal velocity at both interfaces:

$$\frac{d(V_1 + V_2)}{dt} = \int_{A_1} \frac{\partial\Phi}{\partial\zeta_1}\,dA_1 + \int_{A_2} \frac{\partial\Phi}{\partial\zeta_2}\,dA_2. \quad (2.29)$$

3. Numerical implementation

In its final form the problem is mixed elliptic–parabolic. In the Eulerian formulation equations (2.7), (2.8), (2.10) and (2.23) are solved; whereas in the mixed formulation the corresponding equations are (2.10), (2.17), (2.18), (2.19) and (2.23). In both cases the unknowns are the shapes of both bubbles as well as the velocity potential and

normal flux at the two interfaces along with the gas pressure. The main difference is that in the mixed formulation a separate evolution equation is needed for each of the coordinates describing the location of the free surfaces. A brief account of the numerical method used for each formulation is given below. The interested reader is referred to PTM1, PTM2 and Pelekasis (1991) for more details.

3.1. *Integration in time*

As explained in PTM2, the fourth-order explicit Runge–Kutta method was found to be more efficient than the other time-integration schemes tested, at least for the types of problems dealt with here. This is determined by the high accuracy needed, especially towards the late stages of motion, where, as will be seen shortly, the relevant timescale decreases significantly. As a consequence, the time step often has to be decreased as integration in time proceeds. In this study, no systematic way of time step adaptation is used. Instead, the time step is halved and time integration is continued without changing the number of nodal points, whenever a significant loss of accuracy is observed. Subsequently, calculations are repeated with a finer mesh and an even smaller time step and the results are compared.

The use of an explicit scheme favours sequential solution for the unknowns. More specifically, the kinematic and dynamic boundary conditions are used in order to update the shape and potential of the two interfaces and then the integral equation and the adiabatic law are used to calculate new values of the flux at the two interfaces and the gas pressures inside the two bubbles. Consequently, when (2.23) is solved for the flux, given the potential, an integral equation of the first kind is solved. As shown in PTM2 this integral formulation compares favourably with the one leading to an integral equation of the second kind in terms of growth of short waves, since it allows accurate integration for longer time.

3.2. *Integration in space*

For the representation of the dependent variables the B-cubic splines are preferable as described in PTM2. In constructing discretized forms of the governing equations a slightly different approach is followed for the two formulations.

First, in the Eulerian formulation the Galerkin finite element method is used for the discretization of the kinematic and dynamic boundary conditions. Integration by parts eliminates second-order derivatives from the mean curvature term and introduces boundary terms which are set to zero by applying conditions (2.11). Integrals involved in the finite element formulation are evaluated using four Gauss points per element. Thus the numerical error is controlled by the interpolation of the derivatives of the unknown functions and it is $O(h^3)$, where h is the maximum element length. However, for large times higher modes become equally important and the rate of convergence deteriorates. The integral equation (2.23) is discretized using the boundary element methodology, whereby the field point is allowed to coincide with each one of the boundary nodes and the two interfaces are split into elements defined by the same nodes. The procedure for evaluating the various kernels is similar to that given in PTM1. The specific form of the kernels is given in Pelekasis (1991).

Second, in the mixed representation the unknown variables are taken to be functions of the parameter ξ ranging from 1 to N, where N is the number of surface particles. When the mean curvature is expressed as a function of ξ (see Pelekasis 1991) second-order derivatives with respect to ξ cannot be eliminated using integration by parts. Therefore, the Galerkin finite element formalism does not offer any significant advantage. As a simpler alternative collocation is used for the construction of the

discretized equations. Equations (2.17), (2.18) and (2.19) are evaluated at the nodal points using the same B-spline representation as in the Eulerian formulation. However, second-order derivatives of the shape have to be interpolated and this lowers the accuracy of the scheme to $O(h^2)$. Nevertheless this is true only at the initial stages of motion. Later on and as higher modes become more important the two formulations become equally accurate. Furthermore, as the free surfaces become significantly distorted, the mixed formulation is the only one that can capture the motion. Consequently, for maximum numerical efficiency and accuracy the Eulerian formulation should be used initially followed by the mixed formulation towards the last stages. Numerical simulations were conducted with both formulations, but most nonlinear results presented in both parts of this study have been obtained using the mixed formulation, whereas for the linear problem the Eulerian formulation has to be used.

The integral equation is again treated using the boundary element methodology. Kernels and the rest of the terms appearing in the integrand are now expressed in the global coordinate system, see figure 2. The actual expressions in spherical coordinates are given in PTM1 and PTM2. Owing to the acceleration of their centres of mass, the two bubbles may approach or even cross the origin of their respective local coordinate system. Then, in the region around one of the two poles very small values of the radial coordinate are generated, which decreases the accuracy of calculations. In order to remedy this, the origin of the local coordinate systems has to be relocated. For convenience, it is moved to the instantaneous centre of mass of each bubble, see Pelekasis (1991).

3.3. *Numerical accuracy and stability*

Next, the two formulations are carefully examined and compared. For this reason, the evolution of the shapes of both bubbles is calculated for a relatively severe initial disturbance and under conditions that favour rapid deformation. In particular, the ratio of the two radii is set to 1 and the dimensionless distance is set to 2.5. For these values of R and D the two bubbles are located quite close to each other initially. In addition the dimensionless static pressure P_s is 666.66. This value is obtained for air bubbles with radius of the order of 1 mm surrounded by water with far-field pressure 1.0 atm. A radius of 1 mm is assumed, since it has been reported by Kornfeld & Suvorov (1944) as a typical bubble size in their cavitation experiments. A step change in the far-field pressure is applied as initial disturbance with $\epsilon = 0.3$, equation (2.1).

The step change in pressure induces volume oscillations in both bubbles. For infinite initial separation the period of radial oscillation for each bubble is given in dimensionless form as

$$T_{0,\infty} = \frac{2\pi}{\omega_{0,\infty}} = \frac{2\pi}{[6(P_s + 1/R)\gamma/R^2 - 2/R^3]^{\frac{1}{2}}}, \tag{3.1}$$

which for the given set of parameters and polytropic constant, $\gamma = 1.4$, gives $T_{0,\infty} = 0.084$. As will be seen in §4 this value does not change significantly, if the two bubbles are closer at $t = 0$, i.e. if D is initially smaller. Choosing the time step to be 0.0005 requires roughly 170 time steps per period. As a compromise between numerical accuracy and computational cost, 41 points per surface are used. Since the two bubbles are equal in size the plane normal to the z-axis at O is a plane of symmetry and the two free surfaces evolve in exactly the same way.

Using the Eulerian scheme the motion is followed until at $t = 0.47$ computations fail. The total energy increases exponentially fast and the bubble shapes are no longer
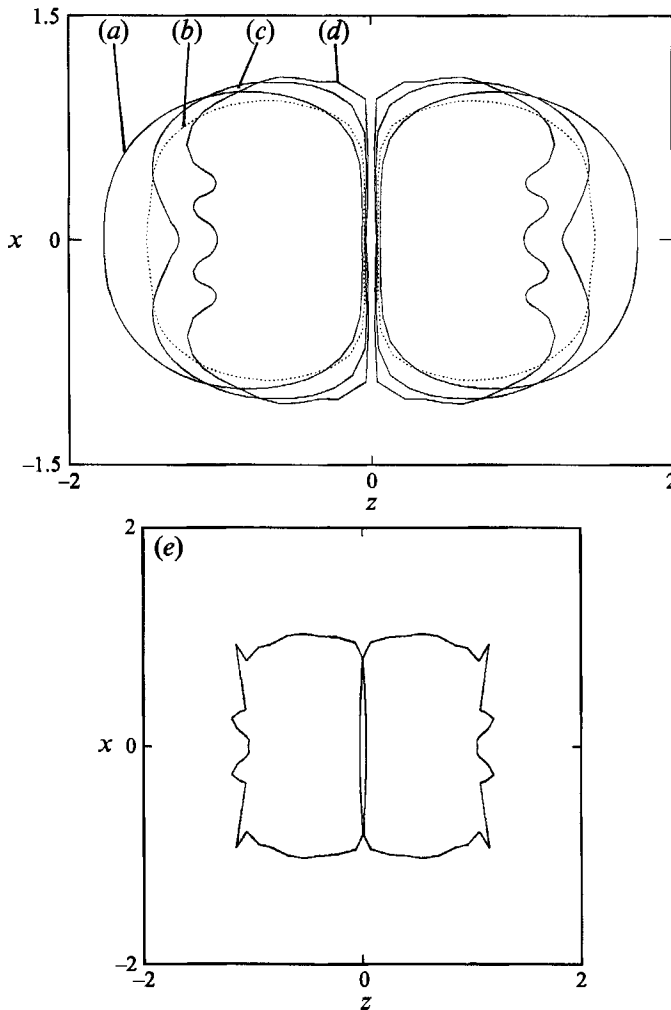
FIGURE 3. Deformed bubble shapes near coalescence with $R = 1$, $D = 2.5$, $\epsilon = 0.3$ and $P_s = 666.66$, at (a) $t = 0.34$, (b) $t = 0.38$, (c) $t = 0.42$ and (d) $t = 0.48$; 41 particles are used per surface with the mixed scheme and $\Delta t = 0.0005$; (e) $t = 0.47$ with the Eulerian scheme. The above parameter values result in an initial average acceleration of $\langle g \rangle = 7.2$.

smooth. Increasing the number of nodal points to 81 and decreasing the time step to $\Delta t = 0.000125$ does not change the results significantly. Using the mixed formulation, and following 41 particles per surface, computations fail a little later at $t = 0.49$; compare figure 3(a–d) to figure 3(e). Energy is now conserved up to the fourth digit until $t = 0.49$ at which point it starts growing exponentially fast. Increasing the number of Lagrangian particles to 81 requires a decrease in the time step to 0.000125 for numerical stability. Again, shapes that are only deformed on the side facing away from the direction of acceleration arise, though they are much smoother now. These shapes will be called spherical-cap shapes. Agreement with results obtained using 41 points is at worst up to two significant digits; this happens near the poles of the bubbles and at $t = 0.49$.

Therefore, although calculations with the mixed formulation proceed slightly further in time, when they fail the results are similar to those obtained with the Eulerian

scheme. In fact in both schemes all the spherical harmonic modes start growing significantly towards the end of computations but at no point do the higher modes become dominant. The Fourier–Legendre modes of the shape are defined with respect to the instantaneous centre of mass of each bubble; Pelekasis (1991). Hence, a short-wave instability of the type found in PTM1 and PTM2 has to be ruled out. The fact that the minimum distance between the two bubbles has become comparable with the average element size can account for some loss of accuracy, but not to this extent. It certainly cannot explain the very pronounced irregularities at the sides of the two interfaces which are opposite to the direction of acceleration. It should also be noted that no significant concentration of nodes, due to the motion of surface particles, was observed. This is in contrast to studies of gravity water waves where the particles tended to segregate and create regions of high and low resolution. Even when we increased the number of nodes in regions of high curvature calculations failed at about the same time. Given the above observations, and others stated in Pelekasis (1991), we conclude that this failure of both numerical schemes is not a numerical artifact. It is due to the Rayleigh–Taylor instability which deforms the accelerating bubble surfaces so severely and abruptly that they cannot be accurately calculated. It will be further demonstrated in §5 that this instability occurs when enough time has elapsed for inertial forces to dominate surface tension forces and give rise to spherical-cap shapes. A similar effect was reported by Harper, Grube & Chang (1972) in their study of the deformation of an accelerating droplet.

As a measure of the computational cost of the simulations, when 41 particles are followed per free surface, roughly 60 CPU seconds are needed per time step on an IBM 3084 and 15 CPU seconds on an IBM 3090. About 90% of this time is consumed in setting up the system matrix and the remaining 10% in factorizing it. As explained in PTM1, by doubling the number of nodal points computation time is a little more than tripled.

4. Normal mode analysis and linear oscillations of equal and unequal bubbles

When the initial disturbance in the far-field pressure becomes negligibly small in comparison to the static pressure, P_s, i.e. $\epsilon \to 0$, the motion becomes almost inertialess for a significant period of time. Then, the Eulerian representation of the governing equations takes the linearized form

$$\nabla^2 \bar{\Phi} = 0, \quad -\infty \leqslant \mu \leqslant \infty, \quad 0 \leqslant \eta \leqslant \pi, \tag{4.1}$$

$$\frac{\partial \bar{f}_i}{\partial t} = \left(\frac{\cosh \mu_i - \cos \eta}{\alpha}\right)^2 \frac{\partial \bar{\Phi}}{\partial \mu}, \quad \mu = \mu_i, \quad 0 \leqslant \eta \leqslant \pi, \quad i = 1, 2, \tag{4.2}$$

$$\frac{\partial \bar{\Phi}}{\partial t} = (-1)^i \frac{1}{\alpha} [2\bar{f}_i \cosh \mu_i + \bar{f}_{i\eta}(-2\sin \eta + \cot \eta \cosh \mu_i - \cot \eta \cos \eta)$$

$$+ \bar{f}_{i\eta\eta}(\cosh \mu_i - \cos \eta)] - 2\bar{P}_{ig} + 2\bar{P}_\infty, \quad \mu = \mu_i, \quad 0 \leqslant \eta \leqslant \pi, \quad i = 1, 2, \tag{4.3}$$

$$\frac{\partial \bar{f}_1}{\partial \eta} = \frac{\partial \bar{f}_2}{\partial \eta} = \frac{\partial \bar{\Phi}}{\partial \eta} = 0, \quad \eta = 0, \pi, \quad -\infty \leqslant \mu \leqslant \infty, \tag{4.4}$$

$$\bar{\Phi} \to 0, \quad \eta \to 0, \quad \mu \to 0, \tag{4.5}$$

where overbars denote linearized quantities. $\bar{P}_\infty$ is zero for normal mode analysis and non-zero when linear oscillations are studied. The exact expressions for $\bar{P}_{1g}$ and $\bar{P}_{2g}$ in terms of $\bar{f}_1, \mu_1$ and $\bar{f}_2, \mu_2$ respectively are given in Pelekasis (1991).

The solution of Laplace's equation in bispherical coordinates may be expressed in terms of a linear combination of Legendre polynomials in η, multiplied by exponential functions of μ. However, in the present case, owing to the complexity of the boundary conditions the eigenfunctions are not given in terms of a single or even a finite number of Legendre polynomials. Rather, an infinite series of Legendre polynomials has to be used. Following Morse & Feshbach (1953) a solution for the potential of the following form is assumed:

$$\bar{\Phi} \equiv e^{\omega t}(\cosh\mu - \cos\eta)^{\frac{1}{2}}X, \quad X \equiv \sum_{k=0}^{\infty} P_k(\eta)(A_k e^{\frac{2k+1}{2}\mu} + B_k e^{-\frac{2k+1}{2}\mu}), \qquad (4.6)$$

where ω is the eigenvalue, and the eigenfunction X is defined above by the infinite summation. The term in the square root is just a scaling pertinent only to the bispherical coordinates. Equation (4.6) satisfies exactly Laplace's equation and the boundary conditions given by (4.4) and (4.5). Differentiating (4.3) with respect to time and substituting for the time derivatives of $\bar{f_1}$ and $\bar{f_2}$ from the kinematic condition, (4.2), yields the differential eigenvalue equation for ω and X in the form of a harmonic oscillator. This equation is too lengthy to be reproduced here, but is given in Pelekasis (1991). Upon appropriate truncation of the infinite series and application of the orthogonality condition, a generalized eigenvalue problem is obtained, see Pelekasis (1991). It is solved numerically, for successively larger values of N (the number of terms retained in the series), until the lower eigenvalues have converged. This procedure is very commonly used with very accurate results (see, for example, Harper *et al.* 1972). In order to test the accuracy of the eigenvalue calculations the eigenfrequencies of each bubble at infinite distance from each other, i.e. $D \to \infty$, are recovered. In this limit the two bubbles cease to affect each other and each one oscillates independently of the other. The eigenfrequencies are given by the well-known formula (Lamb 1932)

$$\omega_{k,\infty} = \left[\frac{(k^2-1)(k+2)}{R_i^3}\right]^{\frac{1}{2}}, \quad k \geqslant 1, \qquad (4.7)$$

where $R_1 = 1$ and $R_2 \leqslant 1$ for the left and right bubbles respectively. In general, the lower eigenmodes can be captured more accurately.

As the distance D increases, μ_1, μ_2 increase also and consequently computations involve larger arithmetic values. Thus, fewer eigenmodes can be accurately captured since higher modes involve larger contributions from higher Legendre polynomials which generate increasingly large numbers. This should have been expected in view of the fact that in this limit one is attempting to solve what is really two decoupled eigenvalue problems, which renders bispherical coordinates unsuitable for representation.

As shown in table 1, numerically computed eigenvalues of interacting bubbles at $D = 10$ are very close to those predicted for individual bubbles by (3.1) for $k = 0$ and by (4.7) for $k = 1, 2, 3, 4, 5$. Clearly, lower eigenfrequencies need a smaller number of Legendre modes in order to be captured accurately. In fact, from some point on, as the order of the polynomials used in the approximation increases these frequencies do not converge any further. Higher modes converge slower and it is necessary to increase N in order to obtain accurate values. The eigenvectors behave similarly although they are more sensitive to the increase in the number of terms retained in the series.

When the distance between the two bubbles is infinite, two frequencies result for each value of the wavenumber, k, one for each bubble. Thus there exist two infinite sets of eigenfrequencies. Eigenvalues for $R = 0.7$ and at distances $D = 5$ and 2.5 are given in

k	Left bubble is deformed ($R_1 = 1$)			Right bubble is deformed ($R_2 = R = 0.7$)		
	$N = 5$	$N = 8$	$N = 10$	$N = 5$	$N = 8$	$N = 10$
0	5569.5938	5569.5938	5569.5939	11605.105	11605.105	11605.105
1	0.88×10^{-7}	0.1×10^{-8}	0.1×10^{-8}	0.98×10^{-6}	0.1×10^{-9}	0.1×10^{-7}
2	12.000551	12.000001	11.999996	34.985527	34.985424	34.985404
3	40.078286	40.000005	39.999997	116.64927	116.61808	116.61808
4	92.999998	90.001050	90.000001	264.91965	262.39077	262.39067
5	207.10562	168.08294	168.00024	547.04429	489.81331	489.79593

TABLE 1. Numerical convergence of ω_k^2 obtained for $P_s = 666.66$, $\gamma = 1.4$ and $D = 10$

Pelekasis (1991). They demonstrate that as D decreases, these two sets of frequencies evolve continuously from their starting values at $D \to \infty$. In fact, the eigenvalues stemming from lower wavenumbers change faster with decreasing D. The one corresponding to the smaller bubble and $k = 0$ is seen to increase as D decreases, whereas the one corresponding to the larger bubble and $k = 0$ is seen to decrease. Thus, with the same parameters as in table 1, ω_0^2 of the left bubble reduces to 5489.42 and 5180.90 at $D = 5$ and 2.5 respectively; whereas ω_0^2 of the right bubble increases to 12093.21 and 14469.92. The two eigenvalues stemming from $k = 1$ always remain zero, attesting to the translational symmetry of the system. Eigenvalues stemming from $k > 1$ seem to increase very slowly as D decreases.

Furthermore, as D decreases, the eigenvectors become more complicated and more Legendre modes are needed for their representation. They may be expressed in a spherical coordinate system with origin the centre of mass of each bubble, and then decomposed in spherical harmonics. The Fourier–Legendre coefficients of each mode are given by

$$c_{ik} = \int_0^\pi \bar{f}_i(\eta) \, P_k(\eta) \sin(\eta) \, d\eta, \quad i = 1, 2. \qquad (4.8)$$

Then, it may be seen that the dominant harmonic is the Legendre polynomial of the same order as the eigenvector corresponding to the eigenvalue obtained at infinite separation. For example, the eigenvalues 12 and 34.985423, corresponding to $k = 2$ for individual bubbles with $R = 1$ and 0.7 respectively, evolve to 12.0001 and 34.98566 when $D = 5$, with eigenvectors that give rise to the shapes shown in figures 4(a) and 4(b). In figure 4(a) the presence of the second Legendre mode, P_2, is evident in the shape of the left bubble whereas the other one remains almost spherical. The opposite is true in figure 4(b). Another important feature of the present problem is that the eigenvectors involve all the spherical harmonics, to a varying extent. Indeed, close examination of figure 4(b) reveals that the ratio between the two volumes is different from the one prescribed by the initial conditions, due to the presence of P_0 that induces volume oscillations.

Table 2 gives the converged eigenfrequencies, along with the number of terms needed for convergence, for two bubbles of equal size, $R = 1$ and at distances $D = 10$, 5 and 2.5 apart. Translational symmetry is still present, hence the two zero eigenvalues for all three values of D when $k = 1$. In this special case, the two infinite sets of eigenfrequencies are identical when $D \to \infty$. However, as D decreases from infinity two eigenfrequencies evolve from each wavenumber $k = 0, 2, 3, 4, \ldots, \infty$. They correspond to the two bubbles oscillating in and out of phase. More specifically the smaller of the two frequencies corresponds to in-phase bubble oscillations, whereas the larger one
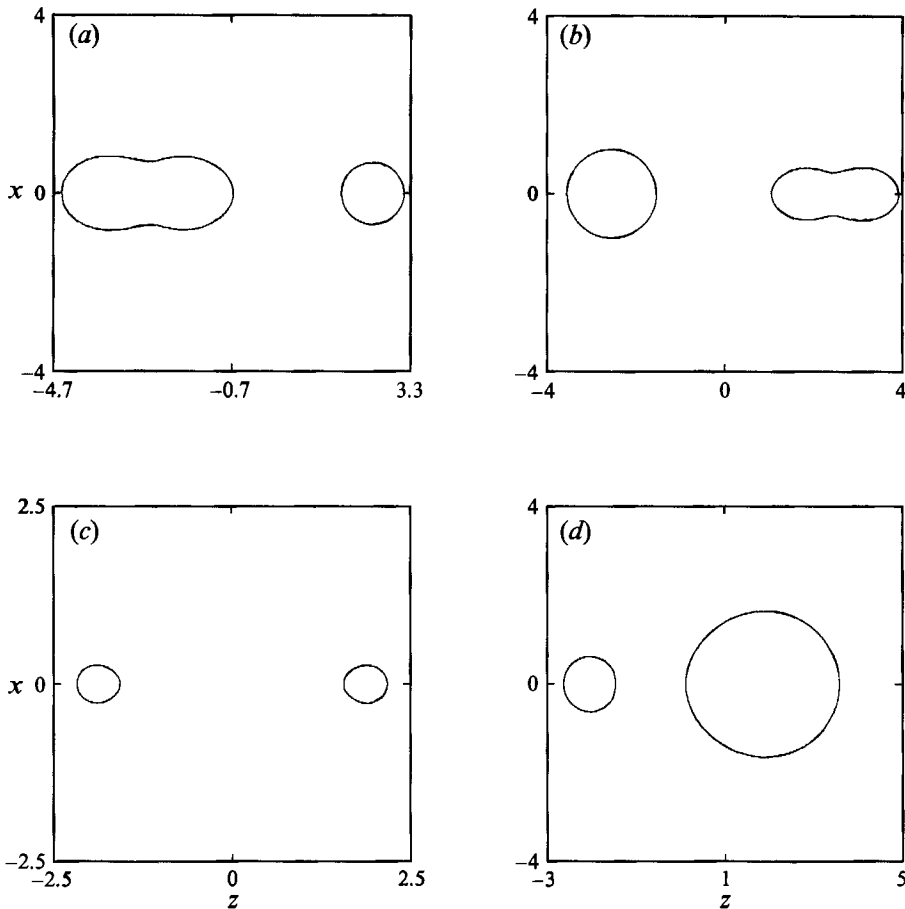
FIGURE 4. Bubble shapes corresponding to selected eigenvectors of the linear problem at $P_s = 666.66$: (a) eigenvector stemming from $k = 2$ at infinite distance with the left bubble deforming, $R = 0.7$ and $D = 5.0$; (b) as (a) but for the right bubble; (c) eigenvector stemming from $k = 0$ at infinite distance corresponding to in-phase oscillations, $R = 1.0$ and $D = 4.0$ and (d) as (c) but corresponding to out-of-phase oscillations.

corresponds to out-of-phase oscillations. Figures 4(c) and 4(d) show the shapes of the two bubbles given by the eigenvectors stemming from $k = 0$ for $D = 4$, $P_s = 666.66$ and $\gamma = 1.4$ when the bubbles oscillate in and out of phase respectively. Moreover, the pattern that was observed for the eigenvalues stemming from $k = 0$ in the case of unequal radii is observed here for the eigenvalues evolving from all wavenumbers. That is, as D decreases, the eigenvalue corresponding to in-phase oscillations decreases, while the other one increases. Similar results have been obtained by Scott (1981), for the eigenvalues stemming only from $k = 0$ for a pair of equal bubbles in the absence of surface tension, and by Sangani (1991), for the linear frequencies of two equal bubbles in the presence of surface tension and in the limit $D \rightarrow \infty$. It was also found that, irrespective of the relative size and distance of the bubbles, decreasing the static pressure decreases the eigenvalues stemming from $k = 0$, whereas the rest do not change significantly. For example, when $P_s = 50$, $\omega_0^2 = 355.82$ and 534.14 for in-phase and out-of-phase oscillations of two equal bubbles at $D = 5$, see Pelekasis (1991).

For relatively small disturbances and during the early stages of the motion even forced oscillations of the two bubbles can be accurately captured by the linearized

	D = 10				D = 5			
	In phase		Out of phase		In phase		Out of phase	
k	ω_k^2	N	ω_k^2	N	ω_k^2	N	ω_k^2	N
0	5097.1435	5	6229.9718	5	4678.3411	10	7022.8218	10
1	0.3×10^{-9}	8	0.3×10^{-9}	8	0.1×10^{-9}	12	0.3×10^{-8}	12
2	11.998802	8	12.00120	8	11.96211	12	12.03892	12
3	39.99986	8	40.0001	8	39.9822	12	40.0180	12
4	89.99999	10	90.0000	10	89.994	12	90.006	12
5	167.999	15	168.000	15	167.998	15	168.0016	15

	D = 2.5			
	In phase		Out of phase	
k	ω_k^2	N	ω_k^2	N
0	4079.5078	15	9970.9041	15
1	0.7×10^{-6}	20	0.9×10^{-6}	20
2	10.881	20	13.372	20
3	37.9	20	42.6	20
4	87.31	25	93.39	25
5	165.0	25	171.0	25

TABLE 2. Converged values of ω_k^2 numerically obtained for $R = 1.0$, $P_s = 666.66$, and $\gamma = 1.4$. N is the number of terms retained for the accuracy shown
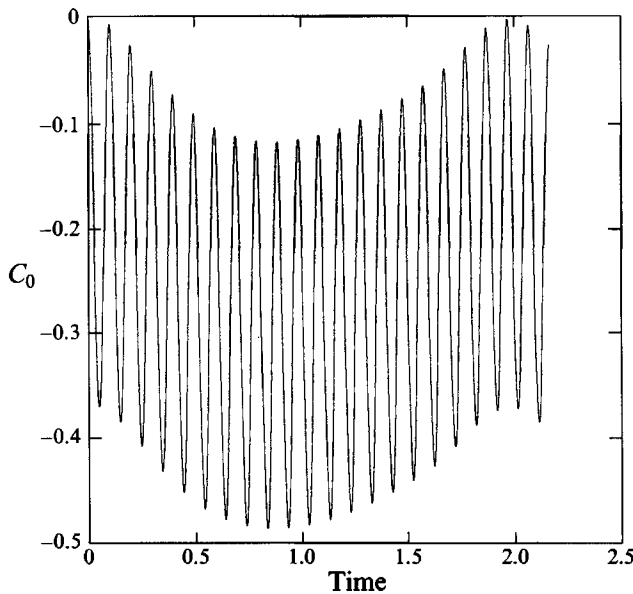
FIGURE 5. Linear oscillations in time of the zeroth Legendre mode with $R = 1$, $D = 2.5$ and $P_s = 666.66$, in response to a step change in the pressure at infinity. Decomposition is done in the original bispherical coordinate system.

problem. For example the linear oscillations of two bubbles of equal size, $R = 1$, located 2.5 radii apart are computed with the initial condition given by (2.1) and $P_s = 666.66$. This excites in-phase oscillations of the two bubbles. Their period, $T_0 = 0.098$, corresponds to $k = 0$ in table 2, see figure 5. At the same time, owing to the presence of other modes the amplitude of $c_0 \equiv \int_0^\pi \bar{f}(\eta) \sin \eta \, d\eta$ is modulated over roughly the linear period of P_2, which is $T_2 = 1.905$, see table 2. Although the centres of mass of each bubble are also oscillating around their initial location, no net attraction between the two bubbles was observed. This should have been expected since the long-term, relative motion of the centres of mass is a nonlinear effect. The dominance of linear volume oscillations during the early stages of the motion is evident in nonlinear calculations as well.

5. Nonlinear oscillations of bubbles with equal radii
5.1. *Global characteristics of the motion*

The time-averaged force between two bubbles of equal radius, undergoing volume oscillations with frequency ω, was known to decrease with the square of the distance between their centres of mass to such early investigators as Bjerknes and Hicks. A straightforward derivation of the average acceleration of the two bubbles, one that avoids the lengthy procedure of the method of images, is given by Batchelor (1967) and Crum (1974). They account for the secondary Bjerknes force on a bubble A, which undergoes only volume oscillations, as a kinematic buoyancy induced by the acceleration of the radiated velocity field from another bubble B, which oscillates with the same frequency. In analogy to gravitational forces, the force on A is given by the product of the acceleration of the fluid in the neighbourhood of A and the volume of fluid that is displaced by this bubble. In other words, the accelerating motion of the two bubbles is really a kinematic effect since no external force is acting on them – the pressure on each surface integrates to zero. Their acceleration will be towards each other when the phase difference in their oscillations, φ, is in the range $0 \leqslant \varphi \leqslant \frac{1}{2}\pi$ or $\frac{3}{2}\pi \leqslant \varphi \leqslant 2\pi$, whereas the two bubbles will move away from each other when $\frac{1}{2}\pi \leqslant \varphi \leqslant \frac{3}{2}\pi$. Finally the acceleration of each bubble, averaged over a period of volume oscillations, is found to depend on the square of the disturbance amplitude ϵ, the inverse square of their distance D, and the square of the oscillation frequency. It should be understood that this is an asymptotic result which holds only in the limit of small initial disturbances, $\epsilon \to 0$, and very large distances, $D \to \infty$. Even though linear quantities were used for obtaining the acceleration, it is an $O(\epsilon^2)$ effect and cannot be captured by solving the linear problem, which is $O(\epsilon)$.

In order to capture this asymptotic behaviour a number of nonlinear numerical simulations were carried out and emphasis was placed on the behaviour of the system during the early stages of the motion. In all cases volume oscillations were induced by a pressure change at infinity. Figure 6 shows the variation with time of the volume of the left bubble for the case of two interacting bubbles of equal size, $R = 1$, with centres located four radii apart initially, $D = 4$. The static pressure P_s is set to 666.66 and this value will be used throughout §5. The effect of the static pressure on the motion is examined separately in §6. Furthermore, the disturbance amplitude, ϵ, is set to 0.2, i.e. the static pressure in the far field is increased at $t = 0$ to $P_\infty = P_s + \epsilon P_s = 799.992$. The volume of each bubble is seen to oscillate in time with constant amplitude and period until at $t \approx 1.2$ it starts increasing exponentially fast, which signals the onset of the Rayleigh–Taylor instability. The volume of the right bubble varies with time in exactly the same way owing to symmetry. From these very regular volume oscillations, or
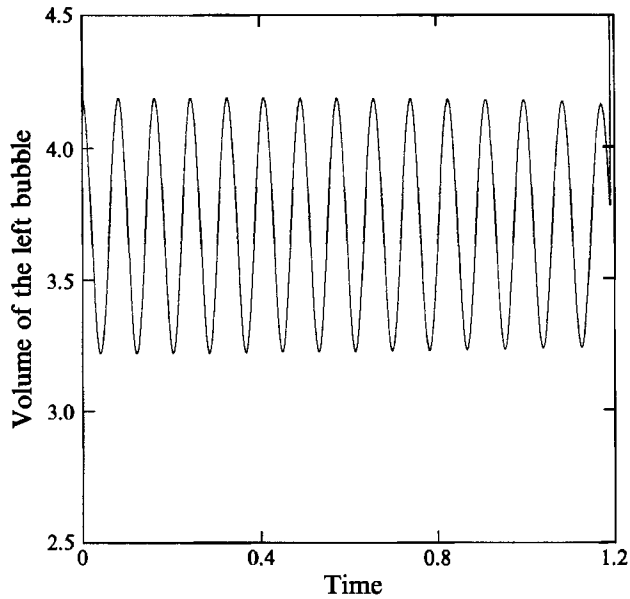
FIGURE 6. Volume oscillations of the left bubble induced by a step change in the pressure at infinity; $\epsilon = 0.2$, $R = 1$, $D = 4$ and $P_s = 666.66$. The right bubble behaves in the same way owing to symmetry.
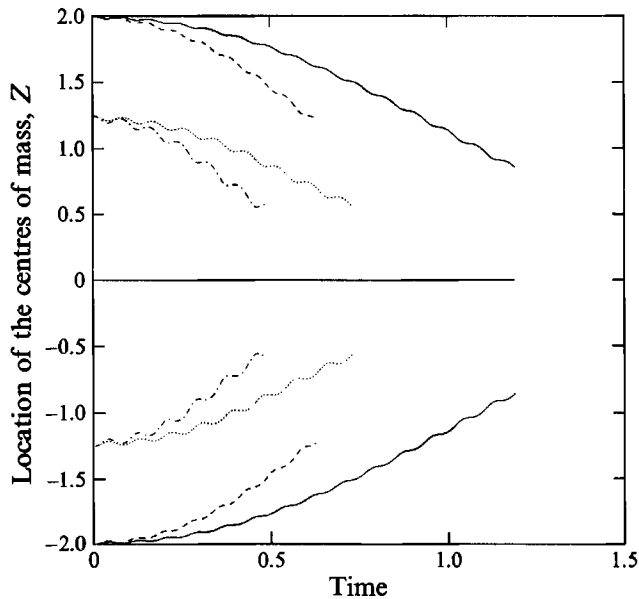

FIGURE 7. Evolution of the centre of mass of the left bubble, $Z_1 \leqslant 0$, the right bubble, $Z_2 \geqslant 0$, and the combined centre of mass, $Z = 0$, until computations break down, for $R = 1$, $P_s = 666.66$, and ———, $D = 4$, $\epsilon = 0.2$; ———, $D = 4$, $\epsilon = 0.3$; ..., $D = 2.5$, $\epsilon = 0.2$ and —·—, $D = 2.5$, $\epsilon = 0.3$.

other 'global' characteristics of the motion, one cannot anticipate the very severe shape deformations that occur under the same conditions after $t \approx 0.9$ which are discussed in §5.2.

Oscillations of the two bubbles are in phase and the period is found to be 0.082, which is lower than the value 0.094 predicted by linear theory for in-phase oscillations
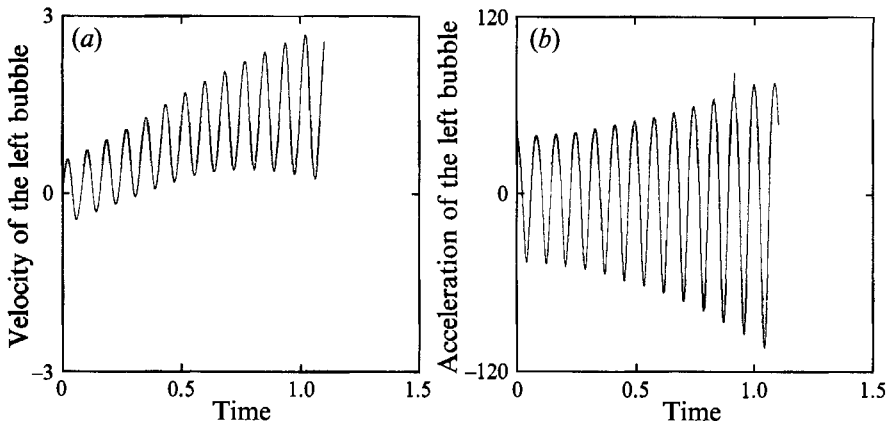
FIGURE 8. Variation with time of (*a*) the velocity and (*b*) the acceleration of the left bubble for $R = 1$, $D = 4$, $\epsilon = 0.2$ and $P_s = 666.66$. The right bubble behaves similarly owing to symmetry.

at $P_s = 666.66$. This is because the zeroth mode is essentially the only eigenmode that is affected by pressure changes. Moreover, an increase in the far-field pressure at $t = 0$ increases the frequency more significantly than inertia decreases it. The latter is a second-order effect (Tsamopoulos & Brown 1983). The same behaviour was reported in PTM1 where the oscillations of a liquid shell are induced by a step change in the exterior pressure. For air bubbles with radius of the order of 1 mm, surrounded by water with density 1 g/cm³ and surface tension 75 g/s², a dimensionless period of 0.082 corresponds to a frequency of 3.3 kHz.

During the early stages of the motion the zeroth eigenmode is predominant and the shapes follow closely the prediction of linear theory. As can be seen from figure 7 the two centres of mass oscillate symmetrically on a fast timescale and keep approaching each other in a slow timescale. The combined centre of mass remains at zero owing to symmetry also, thus confirming the numerical accuracy of the calculations once more. Their velocity and acceleration are also oscillatory and they are shown in figure 8 for the left bubble. The average velocity over a period of volume oscillations is initially increasing almost linearly with time, whereas towards the end of computations it increases at a lower rate. Values for the acceleration have only been obtained up to roughly $t = 1.1$, because numerical accuracy deteriorates beyond this and evaluation of the second time derivative of the location of centres of mass becomes inaccurate. Closer inspection of figure 8(*b*) reveals that the left bubble spends more time accelerating towards the right one than decelerating away from it and, hence, its positive average acceleration over a period. The average acceleration is found to be much smaller than the instantaneous one and has a tendency to remain constant initially. Later it starts decreasing without ever changing its sign, so that the force always remains attractive until computations break down. Indeed, for the current simulation the values of the average acceleration of the left bubble over each of the first 10 periods of its volume oscillation are: $\langle g \rangle = 1.78$, 1.87, 2.05, 1.92, 2.05, 1.75, 1.43, 1.25, 1.03 and 0.68.

The simulation is subsequently repeated with different values of the disturbance amplitude ϵ, and for different initial distances D between the two centres of mass. Numerical values for the average acceleration are given in Pelekasis (1991). They are obtained by averaging over the first period only, because they are seen not to change drastically with time and, in any case, they are the most appropriate ones since the two bubbles deform and approach each other as time increases while asymptotic results
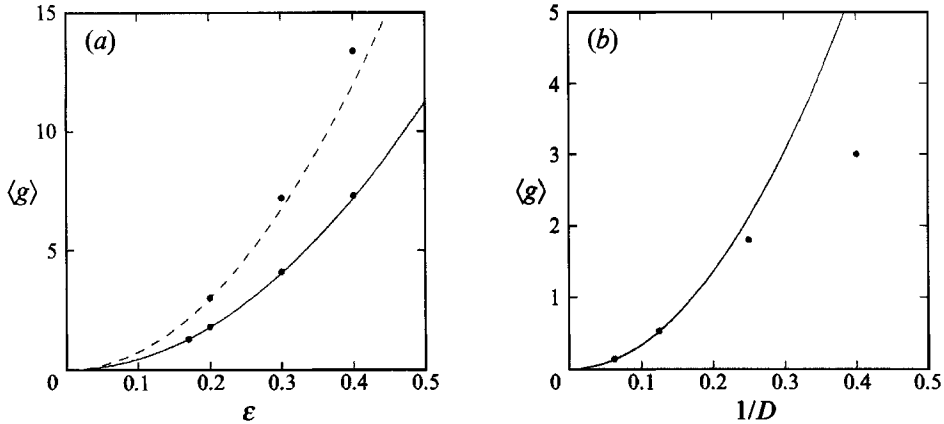
FIGURE 9. Variation of the average acceleration of the left bubble when $R = 1$ and $P_s = 666.66$, with (a) the amplitude of the initial disturbance for $D = 4$, $\langle g \rangle = 13.25\epsilon^2$ (——), and for $D = 2.5$, $\langle g \rangle = 45\epsilon^2$ (——–); and with (b) the initial distance between the two centres of mass for $\epsilon = 0.2$, $\langle g \rangle = 35.84/D^2$. The right bubble behaves in the same way owing to symmetry.

hold in the limit as $D \to \infty$. A graphic representation of the data is given in figure 9(a) along with quadratic curves that fit the points. The curves are produced by assuming an $A\epsilon^2$-type behaviour and calculating the coefficient A using one of the points $(\epsilon, \langle g \rangle)$ found numerically. The cases with $D = 8, 16$ and $\epsilon = 0.2$ are also computed in order to examine the dependence of the acceleration on D. The $O(1/D^2)$ behaviour is followed only when $D \geq 4$ as shown in figure 9(b).

It may be concluded that inertia induces an average motion of the two bubbles towards each other and a constantly increasing velocity. This is a Bernoulli effect and can be explained with essentially the same argument that Kelvin used (Lamb 1932, art. 138) for the attractive force on a stationary body by another one which is oscillating along the line connecting their centres. More specifically, the step change in pressure forces the fluid velocity to be higher in the region between the two bubbles than in the area surrounding them. This is due to the smaller gap between them as compared to the infinite region extending away from the two bubbles. As a result, fluid moves away from the gap and towards the infinite region. Consequently, the two free surfaces are forced to move in such a way as to fill the gap created by the departing fluid, thus bringing the two bubbles closer together. Simultaneously the pressure inside the gap decreases and during the second half of the period higher exterior pressure induces flow towards the gap, until the end of the period when the motion is reversed again. However, for in-phase oscillations and on average, fluid will slowly flow away from the gap and towards infinity. In contrast, when the two bubbles are oscillating out of phase the average fluid motion is directed towards the gap, as will be shown in the second part of this study.

This is opposite to what was observed by PTM1 in the case of an oscillating shell. There, the average velocity eventually changes sign, indicating an oscillatory secondary motion rather than a constantly accelerating one. This difference is attributed to the fact that in the case of a shell there is a symmetric configuration, that of a concentric shell, and the average motion of the two centres of mass is determined by their departure from this configuration. The larger the departure the smaller the average velocity until a maximum in departure is reached where the average velocity changes sign. In the present case the only configuration that would eliminate all asymmetries is that of the two bubbles coinciding at the intersection of the two axes of symmetry.
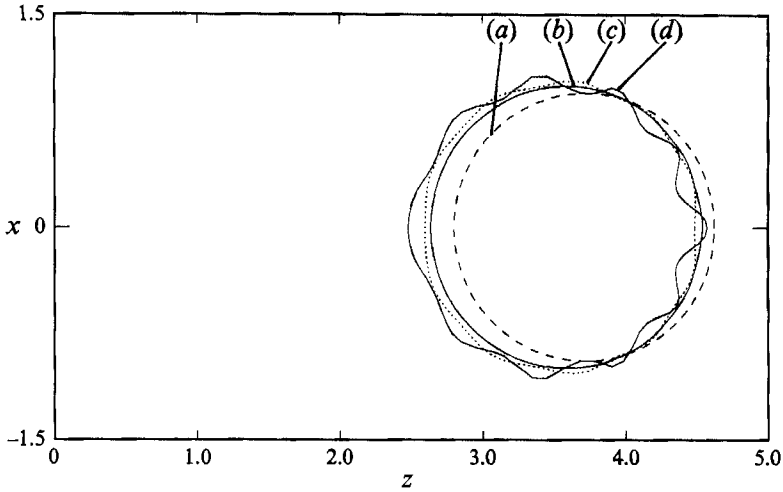
FIGURE 10. Shapes of the right bubble exhibiting globally deformed shapes, up to break down of computations with $R = 1$, $D = 8$, $\epsilon = 0.2$ and $P_{s} = 666.66$, at (a) $t = 1.04$, (b) $t = 1.26$, (c) $t = 1.32$ and (d) $t = 1.40$. These parameter values result in an initial average acceleration of $\langle g \rangle = 0.53$.

This is in fact the configuration that the system is approaching when the two bubbles are accelerating towards each other and it is realized when the two bubbles coalesce to form a new one. Clearly the problem formulation is such that it cannot handle coalescence.

5.2. *Bubble shapes and breakup mechanisms*

As integration in time proceeds and the average velocity of the two centres of mass increases, the evolution of the two interfaces follows two distinct patterns depending on the relative importance of inertia and surface tension, for any given value of P_{s}. Therefore, this evolution is determined by the Bond number, *Bo*. For a pair of equal bubbles this number is identical to the dimensionless average acceleration, $\langle g \rangle$, owing to the scale used for time. *Bo* does not remain constant throughout the motion since $\langle g \rangle$ varies over different periods of the volume oscillations. However, as was seen in the previous section, it does not change significantly and its value during the first period can be used to characterize the motion for all practical purposes.

The effect of acceleration can be made more or less pronounced by changing the initial distance D between the two bubbles, the disturbance ϵ or even the static pressure. In fact, by carrying out a number of numerical simulations it was found that there must be a critical *Bo* beyond which spherical-cap shapes may occur. However, the small variation of $\langle g \rangle$ does not allow for a well-defined value of critical *Bo*. Rather, a critical range of values for *Bo* is identified. More specifically it was found that, when $Bo > 1.5$, spherical-cap shapes appear; whereas when $Bo < 1$ the entire interface deforms. We now present the mechanism that gives rise to both classes of shape.

When $\epsilon = 0.2$ and $D = 8$ the average acceleration is $\langle g \rangle = 0.53$, which is below the critical range. Figure 10 shows the last stage in the evolution of the shape of the right bubble. Clearly, deformation is spread everywhere on both surfaces. The two interfaces evolve in time following a pattern reminiscent of the globally deformed shapes reported by Kornfeld & Suvorov (1944) in their cavitation experiments.

In order to explain the generation of such shapes one needs to examine the evolution of certain coefficients of the Legendre decomposition of the shape of one of the bubbles. Selected coefficients are shown in figure 11. As expected, P_{2} and P_{3} start growing first
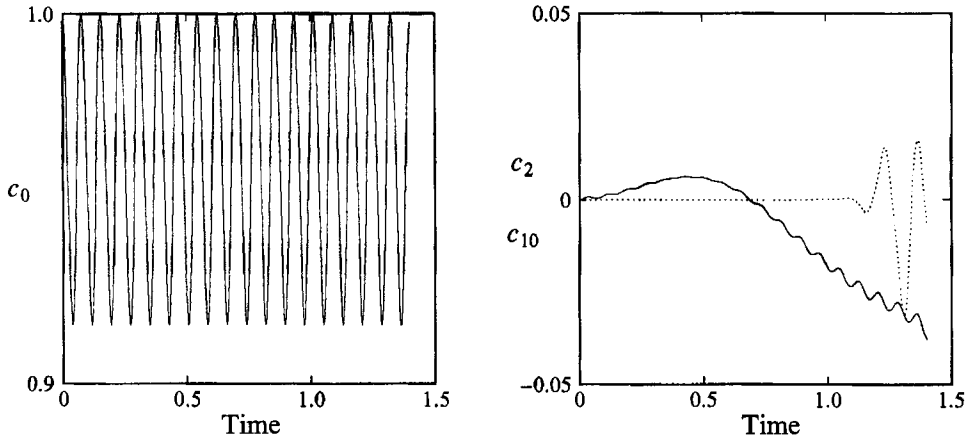
FIGURE 11. Variation with time of selected Legendre coefficients, (a) c_0, (b) ——, c_2; ..., c_{10}, of the shape of the left bubble for $R = 1$, $D = 8$, $\epsilon = 0.2$ and $P_s = 666.66$. The decomposition is done in a spherical coordinate system located on the instantaneous centre of mass of the bubble. The right bubble behaves in the same way owing to symmetry.

through nonlinear interactions. All higher modes remain negligible except for P_9 and P_{10}, which start growing at a later stage but eventually dominate the shape. This can also be seen by noticing the ten lumps developing in the shapes of the two bubbles at $t \approx 1.4$, in figure 10. This is a very interesting effect and can be properly understood in the context of parametric excitation of non-spherical harmonics when the basic radial motion becomes unstable (Hall & Seminara 1980). More specifically, a closer examination of the graphs showing the variation with time of P_0, P_9 and P_{10} reveals that towards the last stages of the motion, but before computations fail, the latter two modes oscillate with a period which is approximately twice the nonlinear period of P_0, $T_0 = 0.078$. Furthermore, linear analysis gives the frequencies of the above modes as $\omega_0 = 70.6$, $\omega_9 = 28.3$ and $\omega_{10} = 34.5$. Hall & Seminara (1980) showed that when the frequency of the radial motion of a single bubble happens to be twice the linear frequency of a Legendre mode and sufficiently large perturbations are applied, subharmonic excitation of the latter mode occurs which eventually dominates the shape of the bubble. This is exactly what is observed here. They also showed that this effect arises on a timescale $O(\epsilon^{-1})$. More emphasis will be placed on the importance of resonance in the dynamic behaviour of the two bubbles in the second part of this study. Eventually computations fail owing to extensive growth of the subharmonically excited modes. Regions of very large curvature are formed at a finite time which are expected to lead to bubble breakup and formation of smaller bubbles under the action of viscosity and surface tension.

Increasing ϵ to 0.4 while leaving the other parameters unchanged increases the Bond number as well, to $Bo = 2.1$. The shapes that arise now are characterized by severe deformation on the side facing away from the direction of acceleration. Hereby, this side will be called the rear side. The other side, correspondingly called the front side, remains almost spherical, figure 12. This configuration is referred to as the spherical-cap shape. Such shapes were originally observed by Davies & Taylor (1950) in their experiments with gas bubbles rising steadily through liquids under the action of gravity. In the second part of this study it will be shown that besides the shape resemblance between the present results and those by Davies & Taylor, in both cases the appearance of such shapes is associated with the balance between inertia and
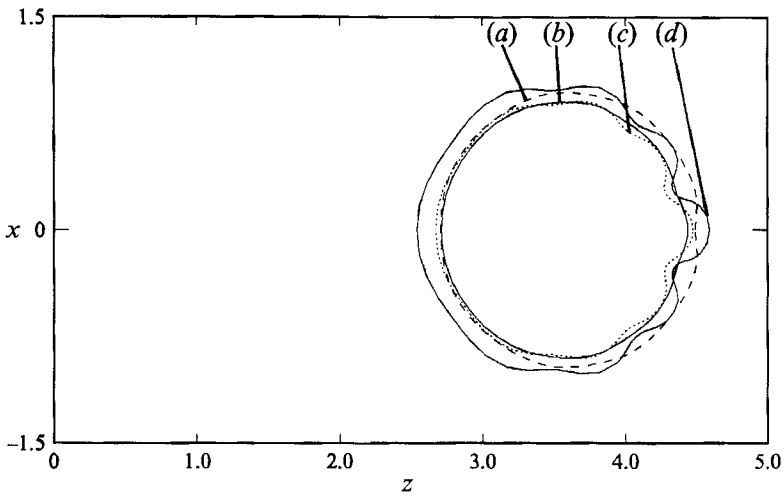
FIGURE 12. Bubble exhibiting spherical-cap shapes, obtained up to break down of computations with $R = 1, D = 8, \epsilon = 0.4$ and $P_s = 666.66$, at $(a)\ t = 0.61, (b)\ t = 0.65, (c)\ t = 0.67$ and $(d)\ t = 0.69$. These parameter values result in initial average acceleration of $\langle g \rangle = 2.1$.
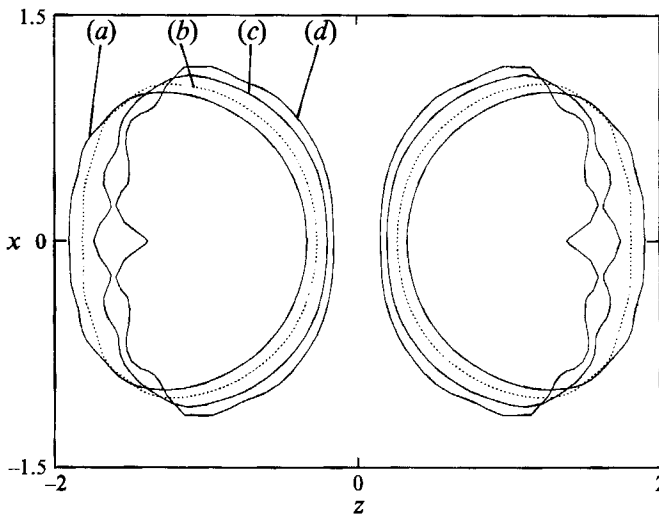

FIGURE 13. Deformed bubble shapes, obtained up to break down of computations with $R = 1$, $D = 4$, $\epsilon = 0.2$ and $P_s = 666.66$, at $(a)\ t = 0.96, (b)\ t = 1.02, (c)\ t = 1.10$ and $(d)\ t = 1.16$. These parameter values result in initial average acceleration of $\langle g \rangle = 1.8$.

surface tension forces and occurs within the same parameter range. It is possible therefore, that the shape evolution observed here may also occur in rising bubbles before they reach their terminal velocity. The Legendre decomposition of the shapes in figure 12 is dominated by the low modes P_2, P_3, P_4, up until computations fail. This behaviour becomes apparent at time $t = 0.7$ which is exactly half the time needed for significant shape deformation to arise when $\epsilon = 0.2$. Repeating the calculation with $\epsilon = 0.5$ yields shapes deformed on the rear sides only and at time 0.6, approximately.

When the bubbles are initially closer together their interaction will be stronger. Figures 13 and 14 show selected shapes for the cases when $R = 1$, $P_s = 666.66$, $D = 4$ and $\epsilon = 0.2$ or 0.3, respectively. In the latter case especially, the shapes obtained
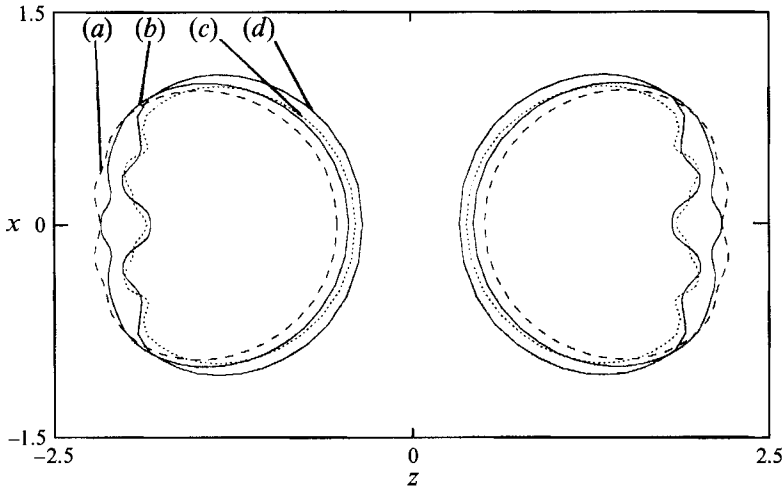
FIGURE 14. Bubbles exhibiting spherical-cap shapes, obtained up to break down of computations with $R = 1$, $D = 4$, $\epsilon = 0.3$ and $P_s = 666.66$, at (a) $t = 0.52$, (b) $t = 0.56$, (c) $t = 0.60$ and (d) $t = 0.62$. These parameter values result in initial average acceleration of $\langle g \rangle = 4.1$.

$D = 8.0$		$D = 4.0$		$D = 2.5$	
ϵ	Time	ϵ	Time	ϵ	Time
0.2	1.4	0.17	1.2	0.2	0.6
0.4	0.7	0.2	1.0	0.3	0.4
0.5	0.6	0.3	0.6	0.4	0.3
—	—	0.4	0.4	—	—

TABLE 3. Variation with ϵ of the approximate time needed for spherical-cap shapes to appear, for different initial separations, $D = 8.0$, 4.0 and 2.5; in all cases $R = 1$ and $P_s = 666.66$

conform strongly to the pattern described above with a well-defined spherical face at the front. In the former case, where the average acceleration is smaller, the shapes are more oblate-like, i.e. prolonged along the plane normal to the z-axis. Repeating the computation for $D = 2.5$ and $\epsilon = 0.3$ results in the shapes shown earlier in figure 3. The rear side is again significantly deformed whereas the front side is flattened around the pole and it is almost perpendicular to the z-axis. This is expected since the (x, y)-plane is a plane of symmetry and hence pathlines lie on it. At the same time, the two bubbles are very close to each other and the motion of fluid particles attached to their front faces will be very similar to the motion on the (x, y)-plane. For all three cases discussed in this paragraph the Bond number is beyond the critical range, see also figure $9(a)$.

In an effort to give a more quantitative description of the motion, the approximate times at which spherical-cap shapes appear are tabulated for different amplitude of the initial disturbance, ϵ, and different values of the initial distance between the centres of mass, D. As can be seen from table 3 this time is roughly inversely proportional to the amplitude ϵ. The validity of this timescaling $(t \sim \epsilon^{-1})$ is reinforced by noticing an interesting similarity between this problem and that of an oscillating shell examined in PTM1 and in Tsamopoulos & Brown (1987). Figure 7 shows the evolution of the two centres of mass for four different pairs of initial disturbance amplitudes and distances between the two centres. Comparing these with the figures showing the evolution of the
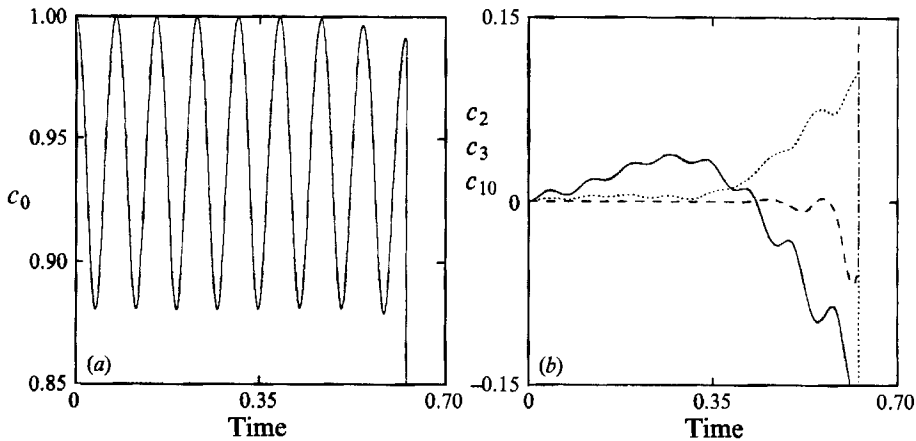
FIGURE 15. Variation with time of selected Legendre coefficients of the shape of the left bubble: (a) c_0, (b) ——, c_2; ..., c_3; ---, c_{10} for $R = 1$, $D = 4$, $\epsilon = 0.3$ and $P_s = 666.66$. The decomposition is done in a spherical coordinate system located on the instantaneous centre of mass of the bubble.

centres of mass of the drop and the bubble in PTM1 one can see that the former resemble the early stages of the oscillatory motion shown in the latter. As explained before, the slow oscillatory motion is absent here since fluid extends to infinity. On the other hand, in the case of a shell, besides the fast oscillation with frequency $\omega_f = O(1)$, the two centres of mass also participate in an oscillatory slow motion with frequency $\omega_s = O(\epsilon)$. When $\omega_f \gg \omega_s$, the amplitude of the oscillations, averaged over one period of the fast motion, can be roughly described as $B\cos\omega_s t$, where B is the amplitude at $t = 0$. Proceeding rather heuristically and expanding around $t = 0$ yields that the amplitude varies as $\frac{1}{2}B\omega_s^2 t^2$. Differentiating twice with respect to time shows that the average acceleration is $B\omega_s^2 = O(\epsilon^2)$. This is constant in time, as is the average acceleration in the present study for most of the motion and for small ϵ. Therefore, the scaling of the acceleration with the square of the disturbance ϵ suggests by analogy that an $O(\epsilon^{-1})$ timescale must exist here as well.

In order to compare the mechanism that generates spherical-cap shapes instead of globally deformed shapes we examine the evolution of certain Legendre–Fourier coefficients with time. This is shown in figure 15 when $\epsilon = 0.3$ and $D = 4$. Additional modes are given in Pelekasis (1991). Comparing the first 40 modes, it is observed that higher and higher modes start growing as time increases, but the lower ones remain dominant. That is $c_i > c_{i+1}$, in general and before computations fail. Eventually, all modes grow exponentially almost simultaneously, just after they start oscillating with the frequency of the zeroth mode. These observations are in sharp contrast to those related to figure 11. As was mentioned in the discussion of numerical stability this growth is not a numerical artifact. It is a result of a Rayleigh–Taylor instability that occurs when the forces of inertia along the direction of motion dominate surface tension forces, hence the critical range of Bond numbers.

Similar shapes were obtained by Harper *et al.* (1972) in their analysis of the motion of a single drop accelerated by the flow of an external gas. The primary timescale in their problem is related to inertia forces and is defined as $t_f = r_0/u_\infty = O(1)$, where r_0 is the radius of the drop at $t = 0$ and u_∞ is the velocity of the exterior gas flow. On this timescale the drop is found to undergo shape oscillations forced by the external gas flow. At the same time, the drop acquires an acceleration g which is $O(\delta)$, where δ is

a measure of the initial disturbance, defined by Harper *et al.* as the ratio ρ_g/ρ_l of the densities of the gas and the drop. This acceleration defines a new timescale $t_s = (r_0/g)^{\frac{1}{2}} = O(\delta^{-\frac{1}{2}})$, which when compared with the fast timescale gives the dimensionless Bond number, $\widehat{Bo} = r_0 g/u_\infty^2 = O(\delta)$. A measure of the relative importance of inertia and surface tension forces, is given in the same study by the Weber number, $\widehat{We} = \rho_l r_0 u_\infty^2/\sigma$. An alternative definition of the Bond number as $Bo = r_0^2 g \rho_l/\sigma$ is used in the present study. Had the latter been used by the above investigators, it would only change their results up to a multiplicative constant, provided that $\widehat{We} = O(1)$. On the slow timescale the effect of acceleration becomes equally important to or even overcomes surface tension and as $\widehat{Bo}$ increases it is seen to give rise to unstable modes. In particular, when a critical lower value of $\widehat{Bo}$ is exceeded an eigenmode with major component the second Legendre polynomial, P_2, becomes unstable. Further increase of $\widehat{Bo}$ excites higher eigenmodes with Legendre polynomials of gradually increasing order as their dominant components. The shape of all the eigenmodes is such that the front face of the drop is almost spherical whereas the rear one is deformed. When $\widehat{Bo}$ is below the critical value, uniformly deformed shapes oscillating in time are obtained. For more details see Harper *et al.* (1972). The pattern in the present study is the same apart from the difference that the average acceleration $\langle g \rangle$ is an $O(\epsilon^2)$ effect. Hence, the timescale on which it becomes important is $O(\epsilon^{-1})$.

The above instability as well as the one encountered here are generalized Rayleigh–Taylor instabilities (Chandrasekhar 1981). That is, by splitting the domain in two and examining each bubble individually, it is found that the fluid surrounding the left bubble has to accelerate as a whole to the left, in view of the motion of the bubble to the right, in order to conserve mass. Then, the instability will appear on the side of the bubble where fluid acceleration is directed from the lighter fluid towards the heavier one. Here, this will happen on the rear side of each bubble.

Another important aspect of this study is the fashion in which computations fail after the onset of the Rayleigh–Taylor instability. Figures 13(d), 14(d) and 3(d) showing spherical-cap shapes during the last stages of computation indicate the formation of troughs and valleys that seem to grow and oscillate in their own right. We have not been able to follow their evolution much further owing to the exponential growth of the eigenmodes. This leads to a curvature singularity at a finite time and before a clear neck is formed; see the rear side of the bubbles at $x = 0$ in figure 13(d). Even though the accuracy of computations decreases when this behaviour appears, the time at which it occurs is found to be the same irrespective of the time step or space discretization used.

This raises the issue of finite-time singularities in potential flow simulations. Baker, Meiron & Orszag (1984) examined the dynamics of an imploding axisymmetric shell in the absence of surface tension. They also observed a singularity in the curvature at a finite time, but before any smooth deformation of the free surface takes place. Pullin (1982) conducted a two-dimensional study on the Rayleigh–Taylor instability of an interface between two immiscible fluids in the presence of gravity and surface tension. He found that even though surface tension stabilized higher modes in the linear limit, nonlinear simulations showed small-scale irregularities before smooth surface deformation occurred. Surface tension simply delayed the appearance of irregularities. In both studies mentioned above, the investigators were concerned with the general reliability of their results. In the present study curvature singularity appears in a finite time and after smooth deformation of the two free surfaces is observed. In addition, mesh and time-step refinement ensure the accuracy of results and relevant experimental

and theoretical studies support our findings. It is anticipated, however, that viscosity will decelerate breakup and allow for a clearer neck formation in regions where deformation is very large, followed by pinch-off in the presence of surface tension.

Now, having obtained the proper scales for the average bubble acceleration ($\langle g \rangle \sim \epsilon^2$) and the time needed for the development of instabilities ($t \sim \epsilon^{-1}$), we can provide a new insight to the experimental observations by Kornfeld & Suvorov. As can be seen from figure 3, when the bubbles are very close initially, coalescence will occur quite fast and it is very unlikely that there will be ehough time for any instability to develop towards breakup. However, as the distance between the two bubbles increases and as it becomes larger than the bubble radius the time needed for coalescence is given roughly as $t = (2D/\langle g \rangle)^{\frac{1}{2}}$, where $\langle g \rangle$ is the average acceleration, taken to be constant with time. Therefore, the quantity $\langle g \rangle t^2$ must become at least $O(1)$, which will happen when time becomes $O(\epsilon^{-1})$ since $\langle g \rangle$ is an $O(\epsilon^2)$ quantity. In other words, coalescence and bubble breakup both occur on the same timescale, which can serve as an explanation for the reduction in size during coalescence observed in the experiments of Kornfeld & Suvorov (1944).

6. Effect of the static pressure, P_s

Increasing the base pressure, P_s, primarily decreases the period of the fast volume oscillations as predicted by linear analysis. When D is sufficiently large, (3.1) gives a very good prediction of the linear period of the volume oscillations which is seen to be decreasing like $P_s^{-\frac{1}{2}}$. As explained before, the initial step change in pressure that induces motion slightly decreases this value. At the same time, owing to the increase in frequency, the average acceleration of the two bubbles should increase proportionally to the pressure P_s. Thus a decrease in both timescales describing the motion should be expected. In order to verify this prediction shapes of the two interfaces for increasing values of the static pressure are calculated, while keeping the other parameters constant. More specifically values of P_s ranging between 190.5 and 5000 are used whereas ϵ, R and D were set to 0.3, 1 and 4 respectively. Setting the bubble size to 1 mm and considering gas bubbles in water, the above range of values for the static pressure covers a wide spectrum of conditions, ranging from 0.3 bar to several atmospheres. The time step was chosen so as to allow for approximately 150 time steps per period of the volume oscillations and 41 points were used for each free surface. Such a wide range of initial conditions and perturbations on them have been used in experiments by Kornfeld & Suvorov (1944) and Crum & Nordling (1972) and are quite common under cavitation conditions (Hammitt 1980).

Table 4 shows the change in the period and the average acceleration as P_s increases. Agreement with the above predictions is gratifying. When $P_s = 190.5$ computations have to stop after roughly 8 periods due to loss of accuracy. The Legendre decomposition of the shape of the left bubble shows significant growth of high modes which makes continuation of the computation impossible (Pelekasis 1991). The shapes obtained do not exhibit any significant deformation even just before collapse, see Pelekasis (1991). The front side is nearly spherical whereas the rear one is more oblate-like and rather flat. For larger values of the static pressure, $P_s \geqslant 666.66$, spherical-cap shapes appear and the calculations break down due to the Rayleigh–Taylor instability. Figure 16 shows the evolution of the shape of the two bubbles when $P_s = 3000$. It is also important that for all cases studied here this behaviour appeared after approximately 8 periods of the volume oscillations. In other words changing the static pressure preserves the major qualitative features of the motion albeit in a different time

P_s	$\langle g \rangle$	T_0
190.5	1.2	0.145
666.66	4.1	0.078
2000.0	12.5	0.045
3000.0	18.7	0.03675
5000.0	31.8	0.0285

TABLE 4. Variation of the average acceleration, $\langle g \rangle$, and the period of volume oscillations, T_0, with increasing static pressure, P_s; in all cases $R = 1$, $D = 4$ and $\epsilon = 0.3$
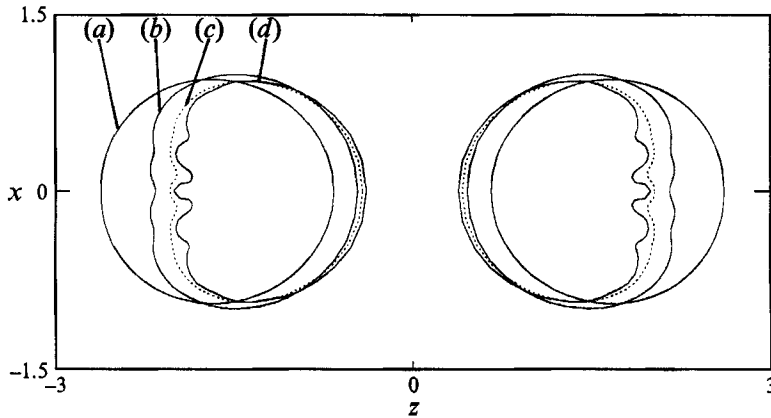

FIGURE 16. Bubbles exhibiting spherical-cap shapes, obtained up to break down of computations with $R = 1$, $D = 4$, $\epsilon = 0.3$ and $P_s = 3000$, at (a) $t = 0.19$, (b) $t = 0.25$, (c) $t = 0.27$ and (d) $t = 0.28$. These parameter values result in initial average acceleration of $\langle g \rangle = 18.7$.
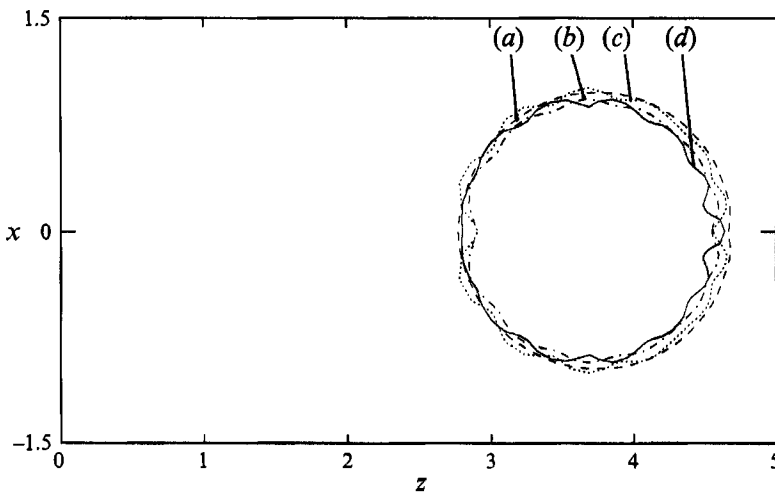

FIGURE 17. Shapes of bubbles exhibiting globally deformed shapes, up to break down of computations with $R = 1$, $D = 8$, $\epsilon = 0.26$ and $P_s = 1500$, at (a) $t = 0.51$, (b) $t = 0.53$, (c) $t = 0.54$ and (d) $t = 0.57$. These parameter values result in initial average acceleration of $\langle g \rangle = 2.0$.
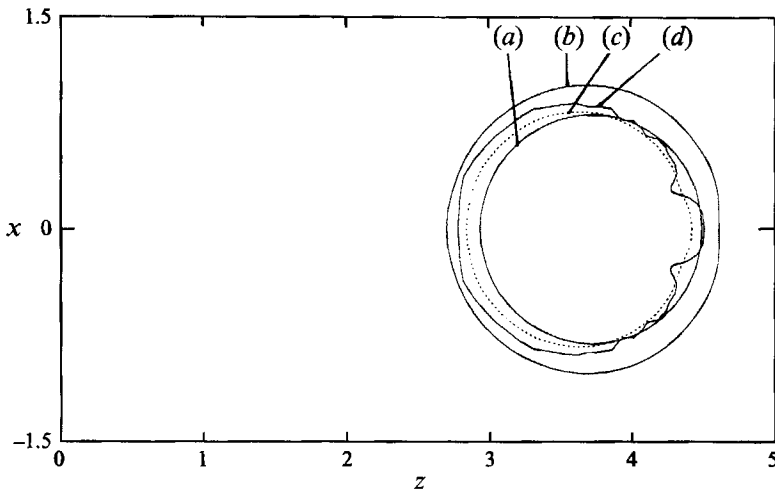
FIGURE 18. Bubble exhibiting spherical-cap shapes, obtained up to break down of computations with $R = 1$, $D = 8$, $\epsilon = 0.6$ and $P_s = 1500$, at (a) $t = 0.23$, (b) $t = 0.25$, (c) $t = 0.27$ and (d) $t = 0.28$. These parameter values result in initial average acceleration of $\langle g \rangle = 10.3$.

frame. It should also be noted that as P_s increases, deformation of the rear side of the bubbles becomes more and more pronounced.

Another important effect of the change in pressure is the shift in the critical Bond number. When $P_s = 666.66$ and for Bond numbers larger than 1.5 spherical-cap shapes occur. Increasing the static pressure to 1500 with $\epsilon = 0.26$, $R = 1$ and $D = 8$ gives rise to severe deformations spanning the entire surface of the two bubbles, figure 17. The Bond number in this case is 2.0. Increasing ϵ to 0.6 and repeating the calculation shows that deformation is now confined to the rear sides of the two bubbles whereas the front sides are slightly flattened, figure 18. The Bond number is roughly 10.3. The times for which the shape deformation becomes apparent for the two values of the disturbance ϵ used are $t = 0.6$ when $\epsilon = 0.26$ and $t = 0.3$ when $\epsilon = 0.6$ and conform to the $O(\epsilon^{-1})$ pattern identified in the previous paragraphs.

Using the results given in table 4 and interpolating, one can deduce that when $\epsilon = 0.3$, $D = 4$ and $P_s = 1500$ the average acceleration $\langle g \rangle = Bo = 9.4$ and spherical-cap shapes will eventually arise. This is in agreement with the range of Bo found above. Hence when $P_s = 1500$ the critical bond number range above which spherical-cap shapes appear is between 2 and 9. This indicates a shift in the critical Bond number towards larger values with increasing static pressure. This may be explained by noticing that the static pressure does not have any preferred direction in space and when it becomes the dominant force it tends to break the bubbles symmetrically. Consequently in order to counteract the effect of larger pressure, larger values of the acceleration are required for spherical-cap shapes to appear.

7. Concluding remarks

In this study the motion of two gas bubbles immersed in an infinite liquid is examined. Motion is induced by a step change in the far-field pressure. The Eulerian formulation is used to solve the linear problem or capture the initial stages of motion, whereas the mixed Eulerian–Lagrangian formulation is used towards the late stages when severe shape deformation occurs. A hybrid method is used for the numerical

solution of the problem. It combines the boundary integral method for Laplace's equation with a weighted residual method (collocation or finite element) for the kinematic and dynamic boundary conditions.

The step change in ambient pressure induces in-phase volume oscillations of the two bubbles that subsequently cause them to accelerate towards each other. Their average acceleration is approximately proportional to the square of the amplitude of the pressure disturbance ϵ, the square of the frequency of volume oscillations and the inverse square of their initial separation.

Owing to the scalings used for making the problem dimensionless, the average acceleration is identical to a Bond number that compares the added inertia due to acceleration to surface tension forces. It is found that when the time becomes $O(\epsilon^{-1})$ these two effects stop balancing each other. This gives rise to significant shape deformations whose nature depends strongly on the magnitude of the acceleration, *Bo*. When *Bo* lies below a critical range of values, deformation is spread everywhere on the two free surfaces and it eventually leads to the formation of smaller bubbles. This is a result of subharmonic resonance between the volume oscillations of the two bubbles and certain non-spherical Legendre modes (Hall & Seminara 1980). When the Bond number lies above this critical range, deformation is confined to the side of the two bubbles facing away from the direction of acceleration. This gives rise to the so-called spherical-cap shapes that have been observed experimentally for gas bubbles rising under the action of gravity (Davies & Taylor). In the latter case, i.e. *Bo* above the critical range of values, the formation of spherical-cap shapes is followed by breakup via a Rayleigh–Taylor instability. This is also confined to the rear side of the bubbles and is identified by exponential growth of the Legendre coefficients of the shape and the development of a curvature singularity at some finite value of time.

Increasing the static pressure causes the critical value of the Bond number to shift to higher values. For example when $P_s = 666.66$ the critical range is found to be $1 \leqslant Bo \leqslant 1.5$ whereas when $P_s = 1500$ the range shifts to $2 \leqslant Bo \leqslant 9$.

Finally, results obtained in the present study are valid until the two bubbles get too close to each other for viscous forces to be ignored. This will happen when time becomes $O(Re^{\frac{1}{2}})$. Therefore, for high *Re* enough time is provided for the phenomena discussed here to evolve. However, in order for the dynamics of coalescence to be studied viscous forces have to be included in the model. This would also allow for a more realistic examination of bubble breakup, since viscosity is expected to modify the effects of the Rayleigh–Taylor instability.

REFERENCES

BAKER, G. R., MEIRON, D. I. & ORSZAG, S. A. 1984 Boundary integral methods for axisymmetric and three-dimensional Rayleigh–Taylor instability problems. *Physica* **12D**, 19–31.

BATCHELOR, G. K. 1967 *Introduction to Fluid Dynamics*. Cambridge University Press.

BENJAMIN, T. B. 1987 Hamiltonian theory for motions of bubbles in an infinite liquid. *J. Fluid Mech.* **181**, 349–379.

BJERKNES, V. F. K. 1906 *Fields of Force*. Columbia University Press.

BJERKNES, V. F. K. 1909 *Die Craftfelder*. Vieweg.

BLAKE, F. G. 1949 Bjerknes forces in stationary sound fields. *J. Acoust. Soc. Am.* 21, 551(l).

CHANDRASEKHAR, S. 1981 *Hydrodynamic and Hydromagnetic Stability*. Dover.

CRUM, L. A. 1974 Bjerknes forces on bubbles in a stationary sound field. *J. Acoust. Soc. Am.* 57, 1363–1370.

CRUM, L. A. & NORDLING, D. A. 1972 Velocity of transient cavities in an acoustic stationary wave. *J. Acoust. Soc. Am.* 52, 294–301.

DAVIES, R. M. & TAYLOR, G. I. 1950 The mechanics of large bubbles rising through extended liquids and through liquids in tubes. *Proc. R. Soc. Lond.* A 200, 375–390.

ELLER, A. I. 1967 Force on a bubble in a standard acoustic wave. *J. Acoust. Soc. Am.* 43, 170–171(L).

HALL, P. & SEMINARA, G. 1980 Nonlinear oscillations of non-spherical cavitation bubbles in acoustic fields. *J. Fluid Mech.* 101, 423–444.

HAMMITT, F. G. 1980 *Cavitation and Multiphase Flow Phenomena*. McGraw-Hill.

HARPER, E. Y., GRUBE, G. W. & CHANG, I-D. 1972 On the breakup of accelerating liquid drops. *J. Fluid Mech.* 52, 565–591.

HICKS, W. 1879 On the problem of two pulsating spheres in a fluid. *Proc. Camb. Phil. Soc.* 3, 276–285.

HICKS, W. 1880 On the problem of two pulsating spheres in a fluid. Part II. *Proc. Camb. Phil. Soc.* 4, 29–35.

KORNFELD, M. & SUVOROV, L. 1944 On the destructive action of cavitation. *J. Appl. Phys.* 15, 495–506.

LAMB, H. 1932 *Hydrodynamics*, 6th edn. Cambridge University Press.

LONGUET-HIGGINS, M. S. & COKELET, E. D. 1976 The deformation of steep surface waves on water, I. A numerical method of computation. *Proc. R. Soc. Lond.* A 350, 1–26.

MILES, J. W. 1977 On Hamilton's principle for surface waves. *J. Fluid Mech.* 83, 153–158.

MORSE, M. P. & FESHBACH, H. 1953 *Methods of Theoretical Physics*. McGraw-Hill.

OGUZ, H. N. & PROSPERETTI, A. 1990 A generalization of the impulse and virial theorems with an application to bubble oscillations. *J. Fluid Mech.* 218, 143–162.

PEARSON, K. 1884 On the motion of spherical and ellipsoidal bodies in fluid media. *Q. Appl. Maths* 20, 60–80.

PELEKASIS, N. A. 1991 A study on drop and bubble dynamics via a hybrid boundary element–finite element methodology. PhD thesis, SUNY at Buffalo.

PELEKASIS, N. A. & TSAMOPOULOS, J. A. 1993 Bjerknes forces between two bubbles. Part 2. Response to an oscillatory pressure field. *J. Fluid Mech.* 254, 501–527.

PELEKASIS, N. A., TSAMOPOULOS, J. A. & MANOLIS, G. D. 1991 Nonlinear oscillations of liquid shells in zero gravity. *J. Fluid Mech.* 230, 541–582 (referred to herein as PTM1).

PELEKASIS, N. A., TSAMOPOULOS, J. A. & MANOLIS, G. D. 1992 A hybrid finite–boundary element method for inviscid flows with free surface. *J. Comput. Phys.* 101, 231–251 (referred to herein as PTM2).

PLESSET, M. S. & HSIEH, D. Y. 1960 Theory of gas bubble dynamics in oscillating pressure fields. *Phys. Fluids* 3, 882–892.

PULLIN, D. I. 1982 Numerical studies of surface-tension effects in nonlinear Kelvin–Helmholtz and Rayleigh–Taylor instability. *J. Fluid Mech.* 119, 507–532.

SANGANI, A. S. 1991 A pairwise interaction theory for determining the linear acoustic properties of dilute bubbly liquids. *J. Fluid Mech.* 232, 221–284.

SCOTT, J. F. 1981 Singular perturbation applied to the collective oscillation of gas bubbles in a liquid. *J. Fluid Mech.* 113, 487–511.

TSAMOPOULOS, J. A. & BROWN, R. A. 1983 Nonlinear oscillations of inviscid drops and bubbles. *J. Fluid Mech.* 127, 519–537.

TSAMOPOULOS, J. A. & BROWN, R. A. 1987 Dynamic centering of liquid shells. *Phys. Fluids* 30, 27–35.

ZAKHAROV, V. E. 1968 Stability of periodic waves of infinite amplitude on the surface of a deep fluid. *J. Appl. Mech. Tech. Phys.* 2, 190–194 (transl. of *Zh. Prikl. Mekh. Tekh. Fiz.* 9(2), 86–94).